Electronic Supplementary Material (ESI) for Physical Chemistry Chemical Physics.

Supporting Information

Reaction-intermediate-induced atomic mobility in heterogeneous metal catalysts for electrochemical reduction of CO_2

Feng Li[a], Ce Zhos[a], Eliana Feygin[a], Pierre-Nicholas Roy[a], Leanne D. Chen[b], Anna Klinkova*[a]*

[a] Department of Chemistry and Waterloo Institute for Nanotechnology, University of Waterloo, Waterloo, ON N2L 3G1, Canada

[b]Electrochemical Technology Centre, Department of Chemistry, University of Guelph, Guelph, Ontario, N1G 2W1, Canada

Mean squared displacement (MSD) calculation

The mean squared displacement (MSD) for coordinate r is time dependent quantity defined as

$$MSD(t) = \langle |r(t) - r(t=0)|^2 \rangle$$

In practice, the ensemble average in the above definition is computed using time averaging and the MSD at some time step t_j is now,

$$MSD(t_j) = \frac{1}{N_i} \sum_{i}^{N_i} \left| r(t_{i+j}) - r(t_i) \right|^2$$

where N_i is the number of time origins used in the averaging procedure. In terms of the simulation time step Δ, the time origins are $t_i = i \cdot \Delta t$.

The coordinate r can be that of a single atom. It can also be a collective coordinate. In the present work, we have have computed the $MSD(t)$ for all the atoms composing the substrate slab and averaged over those atoms. It should be noted that due to the fact the system is only periodic in the two x and y dimensions, only the x and y components are used in the definition of r for the substrate. In the case of the 13 metal atoms forming the initial cluster, the $MSD(t)$ is computed using the full 3-dimensional r vector of each atom. For each simulation, we have identified which of the 13 cluster atoms have the largest $MSD(t)$. For the RIs, the centre-of-mass of the RI was used as a coordinate.

Velocity autocorrelation function

The velocity autocorrelation function is defined as

$$C_{vv}(t) = \langle v(t=0) \cdot v(t) \rangle$$

where the velocity vector at time t, $v(t)$, is correlated to its value at time zero. The ensemble averaging is performed using the time averaging procedure described above for the MSD calculations. We have computed the velocity of the RI's Center of Mass (CMRI) in the present calculations. The $C_{vv}(t)$ correlation function is related to the RI's contribution to the density of states (DOS) via a Fourier transform.

Radial distribution function

The radial distribution function for a system of N atoms is defined as

$$g(r) = C\sum_{i<j}\langle\delta(r - r_{ij})\rangle$$

where C is a proportionality factor and r_{ij} is the distance between atoms i and j. The sum is over all pairs of atoms and the ensemble averaging is performed via time averaging as above. We have separately computed the $g(r)$'s of the substrate atoms, and those of the 13 metal atom clusters, and that of the atom distances of the RI's. The radial distribution function is a measure of the solid-like or liquid-like nature of a system. We observe that for the substrate, the $g(r)$ is that of a solid lattice in good agreement with literature values[1]. For the 13 atom clusters, the $g(r)$ is much less structured due to the fluxional nature of the cluster where the atoms are more mobile. As and additional measure of atom mobility, we have also computed the Lindemann index of the substrate and cluster atoms. The Lindemann index is defined as:

$$\lambda = \frac{1}{N-1}\sum_{i<j}\frac{\sqrt{\langle r_{ij}^2\rangle - \langle r_{ij}\rangle^2}}{\langle r_{ij}\rangle}$$

The quantity λ is measure of how much the distance between a specific pair of atoms can grow. In a solid, atoms stay around their lattice sites and λ is small. However, for a system where atomic mobility is increased, λ will be larger. This is observed for the 13 atom clusters. For all the systems studied here,

$\lambda_{cluster}$ is 2 to 3 times larger than $\lambda_{substrate}$. This is a clear indicator of the enhanced mobility of the cluster atoms compared to their substrate counterpart.

Heat capacity calculation

The speed $v_j(t)$ of the *j*th metal atom at reaction time *t* was calculated as follows:

$$v_j(t) = \sqrt{v_{jx}(t)^2 + v_{jy}(t)^2 + v_{jz}(t)^2}$$

where $v_{jx}(t)$, $v_{jy}(t)$, and $v_{jz}(t)$ are the speeds of the *j*th metal atom along *x*, *y*, and *z* directions.

The kinetic energy $E_{KE_j}(t)$ of the *j*th atom at time *t* was calculated as follows:

$$E_{KE_j}(t) = \frac{1}{2} m_j v_j(t)^2$$

where m_j is the mass of the *j*th metal atom.

The kinetic energy $E_{KE}(t)$ of the whole metal system at the reaction time *t* is the sum of the kinetic energy of each atom,

$$E_{KE}(t) = \sum_j E_{KE_j}(t)$$

Therefore, the total energy $E_{tot}(t)$ of the whole system at reaction time *t* was calculated as follows:

$$E_{tot}(t) = E_{KE}(t) + E_{PE}(t)$$

where $E_{PE}(t)$ is the potential energy of the whole metal system, which can be collected from VASP output.

The total energy $E_{tot\_a}(t)$ of each atom at reaction time *t* was set to be

$$E_{tot\_a}(t) = E_{tot}(t)/n$$

where *n* is the number of the metal atoms in the system.

The heat capacity C_V of the metal system at the reaction time *t* was calculated according to the following equation:

$$C_V = \frac{< E_{tot\_a}(t)^2 > - < E_{tot\_a}(t) >^2}{k_B T_{sys}^2} * n$$

where $< E_{tot\_a}(t)^2 >$ is the expected value of the squared $E_{tot\_a}(t)$ and $< E_{tot\_a}(t) >^2$ is the square of the expected value of $E_{tot\_a}(t)$. They were calculated as follows:

$$< E_{tot\_a}(t)^2 > = \frac{\sum_{t=t_1}^{t=t_2} E_{tot\_a}(t)^2}{m}$$

$$< E_{tot\_a}(t) >^2 = \left[\frac{\sum_{t=t_1}^{t=t_2} E_{tot\_a}(t)}{m}\right]^2$$

where m is the number of the reaction steps between t_1 and t_2 . t_1 and t_2 are the time points when the system first reaches an equilibrated state, and when the simulation was finished, respectively.

Supplementary Note 1

To estimate the influence of the chemical potential on the free energy difference between the HER, the ORR, and the CO2RR pathways, we start from the corresponding adsorption reactions. For the HER reaction, we have:

$M(surf) + H^+(aq) + e^- \rightleftharpoons M * H(ads), \Delta G_{HER}$

Similarly, for ORR and CO_2RR, we have:

$M(surf) + H^+(aq) + O_2(aq) + e^- \rightleftharpoons M * OOH(ads), \Delta G_{OOR}$

$M(surf) + H^+(aq) + CO_2(aq) + e^- \rightleftharpoons M * COOH(ads), \Delta G_{CO_2RR}$

The effect of the chemical potential is brought by chemical equilibrium in a dilute solution:

$$\Delta G_r = \Delta G_r^0 + \sum_i n_i RT ln\left(\frac{C_i}{C^0}\right) \quad \text{(S1)}$$

In eqn (S1), n_i, C_i is the index and the concentration of the i[th] species in the chemical equation. C^0 is the standard concentration, which is 1 mol/L. R is the ideal gas constant and T is the temperature of the

system. For simplicity, we only consider the contribution of aqueous species and the division over C^0 is omitted. Thus, the three relations are established:

$$\begin{aligned} \Delta G_{HER} &= \Delta G_{HER}^{0} - RTlnC_{H+} \\ \Delta G_{OOR} &= \Delta G_{OOR}^{0} - RTlnC_{H+} - RTlnC_{O_2} \\ \Delta G_{CO_2RR} &= \Delta G_{CO_2RR}^{0} - RTlnC_{H+} - RTlnC_{CO_2} \end{aligned} \quad \text{(S2)}$$

Since we are interested in the relative stability of the three adsorbents, the free energy difference of the three reaction pathways should be calculated:

$$\begin{aligned} \Delta G_{OOR} - \Delta G_{HER} &= \Delta G_{OOR}^{0} - \Delta G_{HER}^{0} - RTlnC_{O_2} \\ \Delta G_{CO_2RR} - \Delta G_{HER} &= \Delta G_{CO_2RR}^{0} - \Delta G_{HER}^{0} - RTlnC_{CO_2} \\ \Delta G_{CO_2RR} - \Delta G_{OOR} &= \Delta G_{CO_2RR}^{0} - \Delta G_{OOR}^{0} - RTln\left(\frac{C_{CO_2}}{C_{O_2}}\right) \end{aligned} \quad \text{(S3)}$$

As is suggested in this work, we use binding energies of the adsorbents calculated from eqn (1) to determine their relative stability, and the chemical potential is neglected. The corresponding equations are:

$$\begin{aligned} \Delta G_{OOR} - \Delta G_{HER} &\approx \Delta G_{OOR}^{0} - \Delta G_{HER}^{0} \approx E_{b,OOR} - E_{b,HER} \\ \Delta G_{CO_2RR} - \Delta G_{HER} &\approx \Delta G_{CO_2RR}^{0} - \Delta G_{HER}^{0} \approx E_{b,CO_2RR} - E_{b,HER} \\ \Delta G_{CO_2RR} - \Delta G_{OOR} &\approx \Delta G_{CO_2RR}^{0} - \Delta G_{OOR}^{0} \approx E_{b,CO_2RR} - E_{b,OOR} \end{aligned} \quad \text{(S4)}$$

Substituting the eqn (S4) to eqn (S3), one obtains the following set of equations in which the chemical potential is considered:

$$\begin{aligned} \Delta G_{OOR} - \Delta G_{HER} &\approx E_{b,OOR} - E_{b,HER} - RTlnC_{O_2} \\ \Delta G_{CO_2RR} - \Delta G_{HER} &\approx E_{b,CO_2RR} - E_{b,HER} - RTlnC_{CO_2} \\ \Delta G_{CO_2RR} - \Delta G_{OOR} &\approx E_{b,CO_2RR} - E_{b,OOR} - RTln\left(\frac{C_{CO_2}}{C_{O_2}}\right) \end{aligned} \quad \text{(S5)}$$

If our proposition is valid, the last term in eqn (S5) (namely E_{corr}) brought by the inclusion of chemical potential should be smaller in magnitude than the binding energy difference, ΔE_b, calculated from the first two terms. As the CO_2RR is carried out mainly under ambient condition (298.15K, 1 atm) with constant CO_2 supply, we assume CO_2 is saturated in the electrolyte (615 ppm) while O_2 only reaches 21% of its saturation concentration (4.81 ppm) based on the O_2 content in the atmosphere. Using water's density (0.99705 g/cm^3) and molar mass (18.015 g/mol) under that condition, we then convert the

concentration of the gaseous species to mol/L and calculate E_{corr}. Note that the saturation concentration of the gaseous species and the property of water is from CRC Handbook of Chemistry and Physics[2]. The result of the calculation is summarized in Table S1.

Table S1. Summary of the chemical potential correction calculation

ΔG_r difference	ΔE_b magnitude (eV) [a]	Chemical potential correction, E_{corr}		magnitude ratio (%)[b]
		Value (eV)	Formula	
$\Delta G_{OOR} - \Delta G_{HER}$	1.0	0.211	$-RTlnC_{O_2}$	21.1
$\Delta G_{CO_2RR} - \Delta G_{HER}$	0.2	0.028	$-RTlnC_{CO_2}$	13.9
$\Delta G_{CO_2RR} - \Delta G_{OOR}$	1.2	-0.184	$-RTln(C_{CO_2}/C_{O_2})$	15.3

[a]visually estimated from Figure 1b

[b]calculated as $|E_{corr}/\Delta E_b| \times 100\%$

From table S1, we can see that the magnitude of E_{corr} is on average around 16% of the calculated binding energy difference. In the case involving only the relatively dilute oxygen, the correction is the most significant.

Sample calculation

Converting concentration of CO_2 in ppm to mol/L:

$$C_{CO_2} = 615\ ppm$$

$$= 6.15 \times 10^{-4} \times \frac{1L \times 997.05g\ L^{-1}}{18.015g\ mol^{-1} \times 1L}$$

$$= 3.40 \times 10^{-1} mol\ L^{-1}$$

Calculate E_{corr} for $\Delta G_{CO_2RR} - \Delta G_{HER}$

$$E_{corr} = -RTlnC_{CO_2}$$

$$= -8.3145\ J\ mol^{-1}K^{-1} \times 298.15\ K \times \ln(0.340)$$

$$= 1.08\ J\ mol^{-1} = 0.0277\ eV \approx 0.028\ eV$$

The magnitude ratio:

$$Ratio = \left|\frac{E_{corr}}{\Delta E_b}\right| \times 100\% = \left|\frac{0.028\ eV}{0.2\ eV}\right| \times 100\% = 13.9\%$$

Supplementary Note 2

The size of a metal cluster has a significant effect on its stability, with the stability of the nanoparticle increasing with increasing the cluster size, which has been well explored both experimentally[3] and theoretically[4]. However, here, we focus on the effect of the RIs on the stability of the metal cluster. To reveal the effect of the RIs efficiently, a suitable size of the metal cluster has to be selected considering the dependence of the metal cluster's stability on its size and the high computational cost of AIMD. A 13-atom metal cluster allow us to differentiate the effect of the RIs on the stability of the metal cluster while remaining a reasonable computational demanding. First, a metal cluster with less atoms is not structurally stable on a support, which tends to dissolute and redeposit on the surface of the support due to the Ostwald ripening effect[5]. On the contrary, a cluster with more atoms becomes too computationally demanding. For example, COOH-bound Au atom was observed to be extracted from a 13-atom Au cluster at around 0.7 ps, while it was not observed on an 18-atom Au cluster even after 2 ps. (Figure S21) Therefore, to evaluate the effect of the RIs on a cluster with more atoms, longer AIMD simulations are required, which makes this theoretical evaluation approach more computationally expensive.

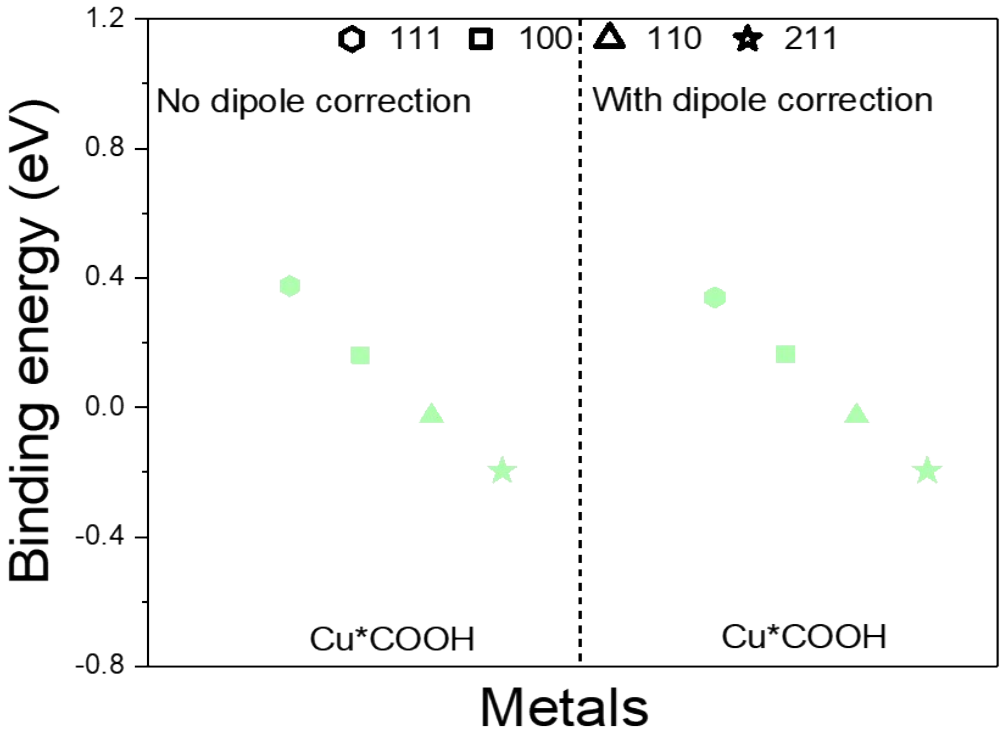

Figure S1. Effect of the dipole correction on the surface adsorption calculations using DFT.

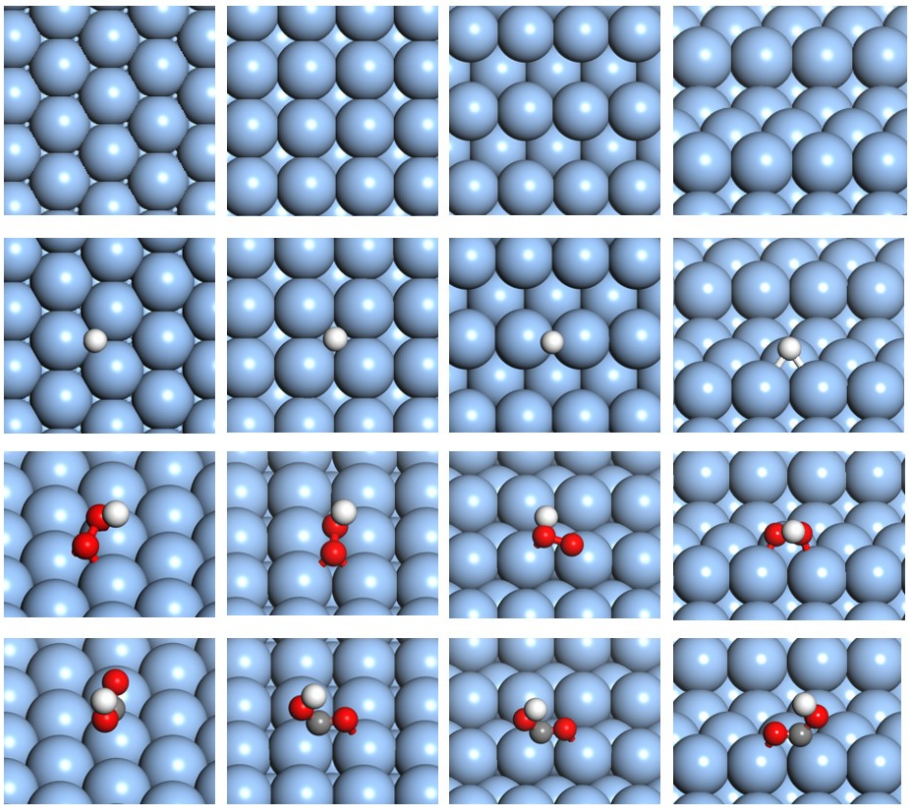

Figure S2. the optimized geometries of Ag(111), Ag(100), Ag(110), and Ag(211) surfaces without (top panels) and with (bottom panels) absorbed *H, *OOH and *COOH.

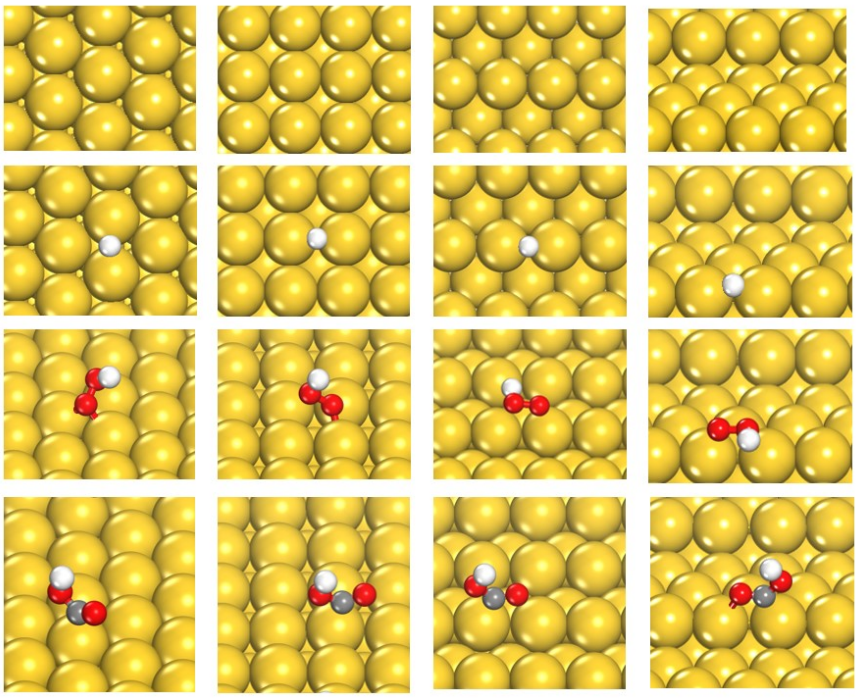

Figure S3. the optimized geometries of on Au(111), Au(100), Au(110), and Au(211) surfaces without (top panels) and with (bottom panels) absorbed *H, *OOH and *COOH.

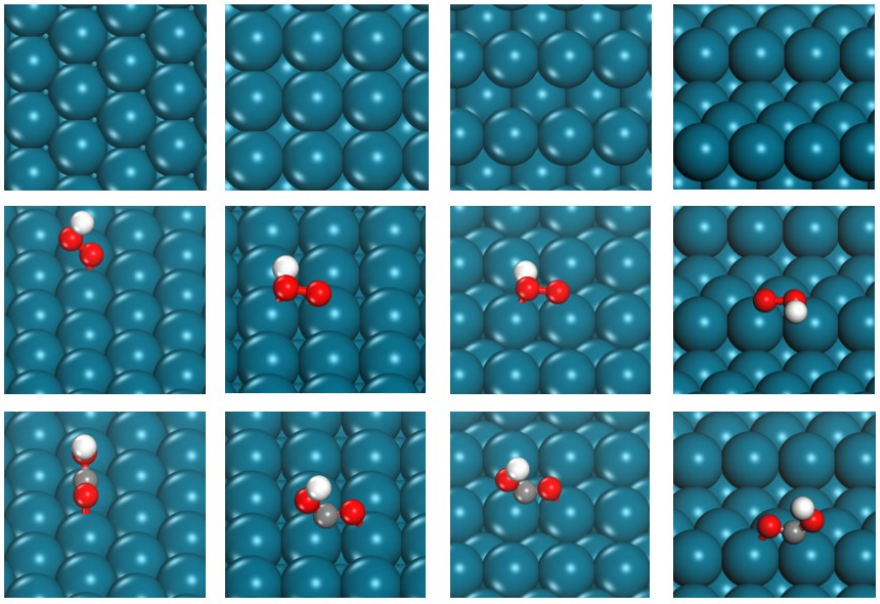

Figure S4. the optimized geometries of Pd(111), Pd(100), Pd(110), and Pd(211) surfaces without (top panels) and with (bottom panels) absorbed *OOH and *COOH.

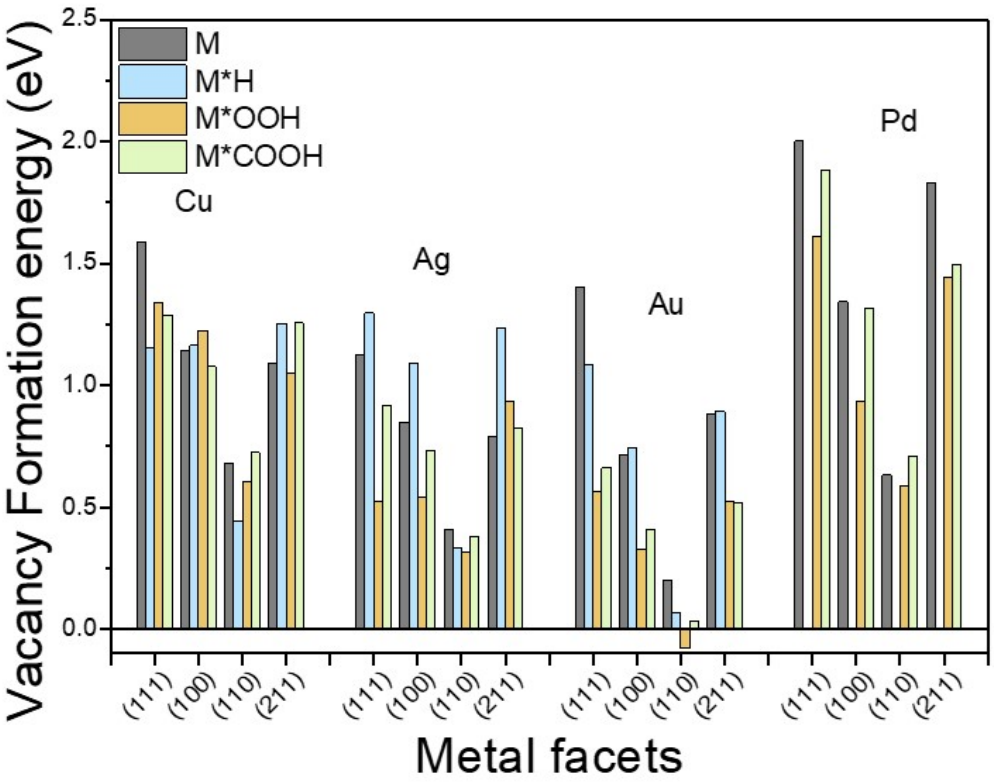

Figure S5. The influence of the reaction intermediates and metal materials on vacancy formation energy. The (111), (100), (110), and (211) surfaces of Cu, Ag, Au, and Pd were studied with and without adsorbed RIs.

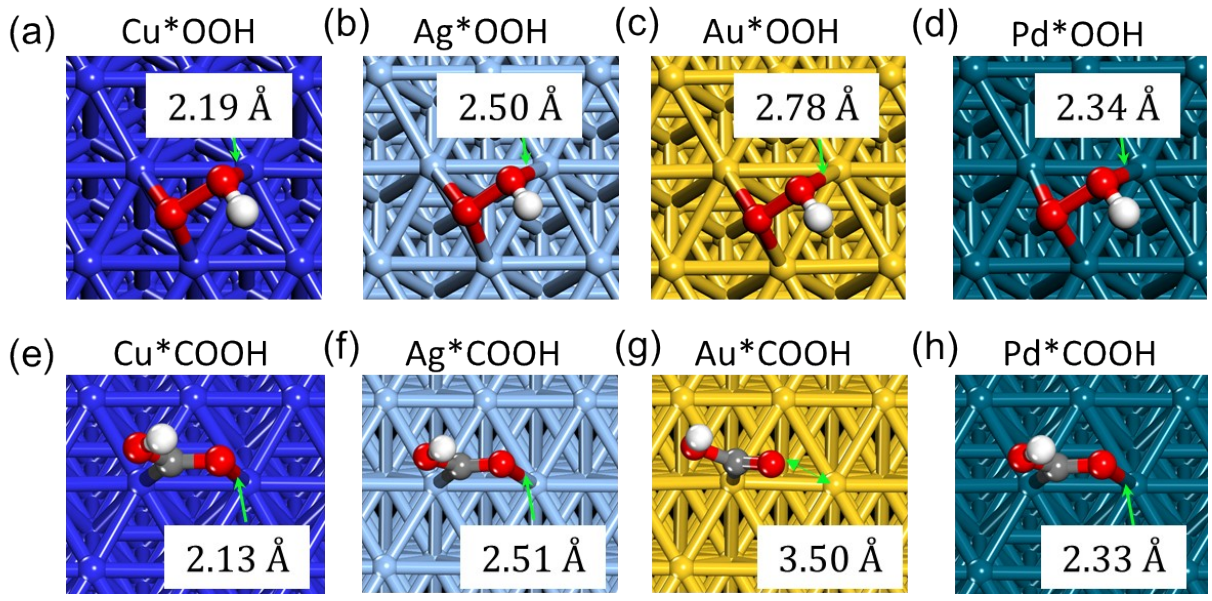

Figure S6. Comparison of the adsorption structures for *OOH and *COOH on Cu(111), Ag(111), Au(111), and Pd(111) without vacancy.

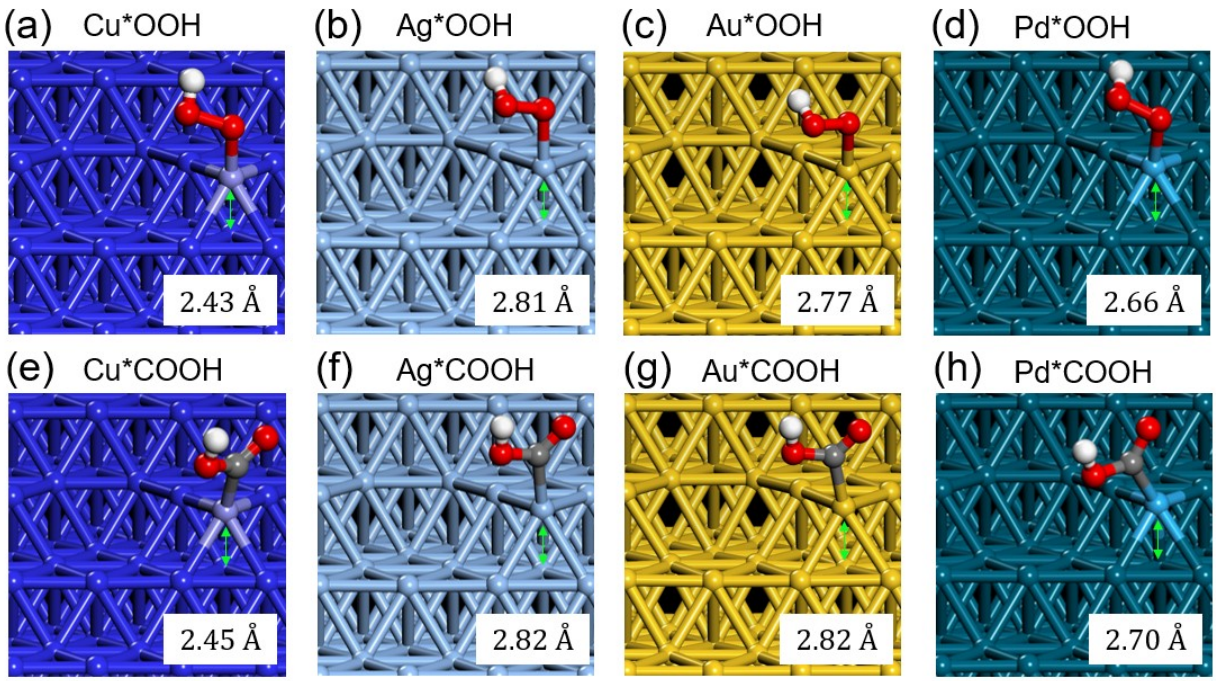

Figure S7. Comparison of the adsorption structures for *OOH and *COOH on Cu(111), Ag(111), Au(111), and Pd(111) with single-atom vacancy.

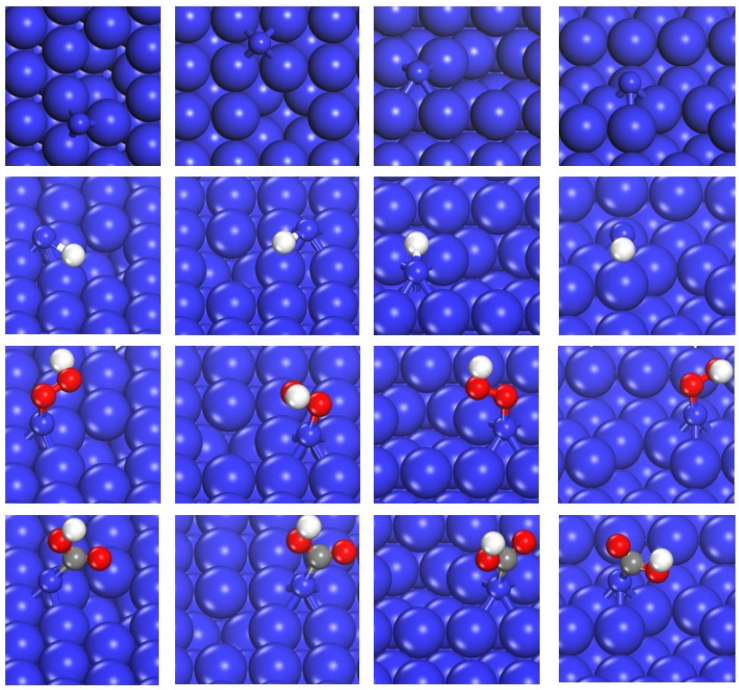

Figure S8. The optimized singe-atom vacancy on Cu(111), Cu(100), Cu(110), and Cu(211) surfaces without (top panels) and with (bottom panels) absorbed *H, *OOH and *COOH.

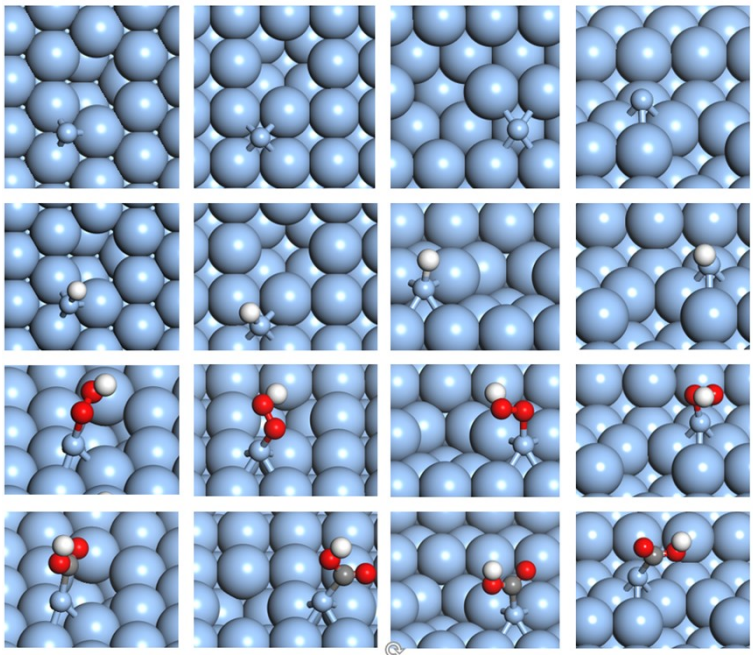

Figure S9. The optimized singe-atom vacancy on Ag(111), Ag(100), Ag(110), and Ag(211) surfaces without (top panels) and with (bottom panels) absorbed *H, *OOH and *COOH.

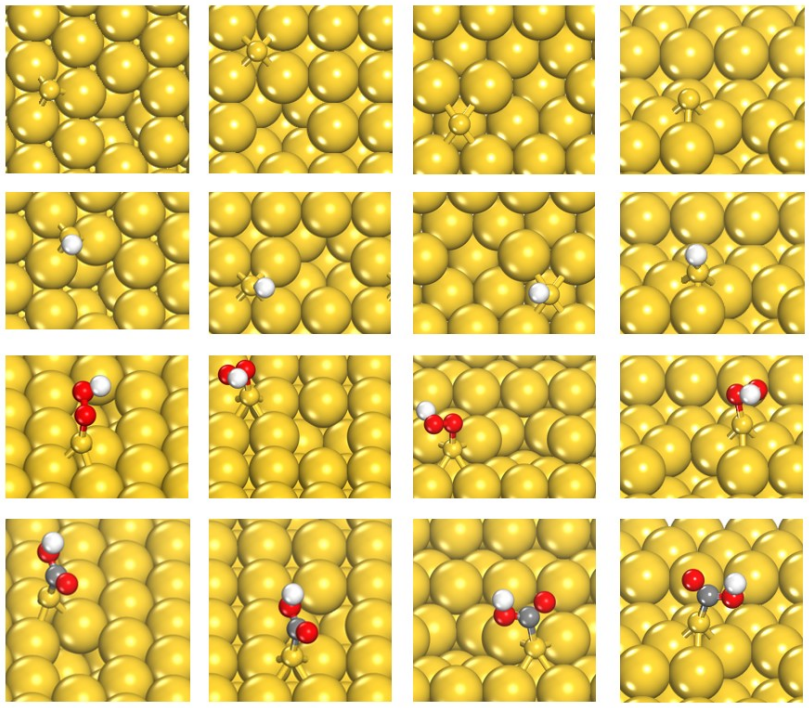

Figure S10. The optimized singe-atom vacancy on Au(111), Au(100), Au(110), and Au(211) surfaces without (top panels) and with (bottom panels) absorbed *H, *OOH and *COOH.

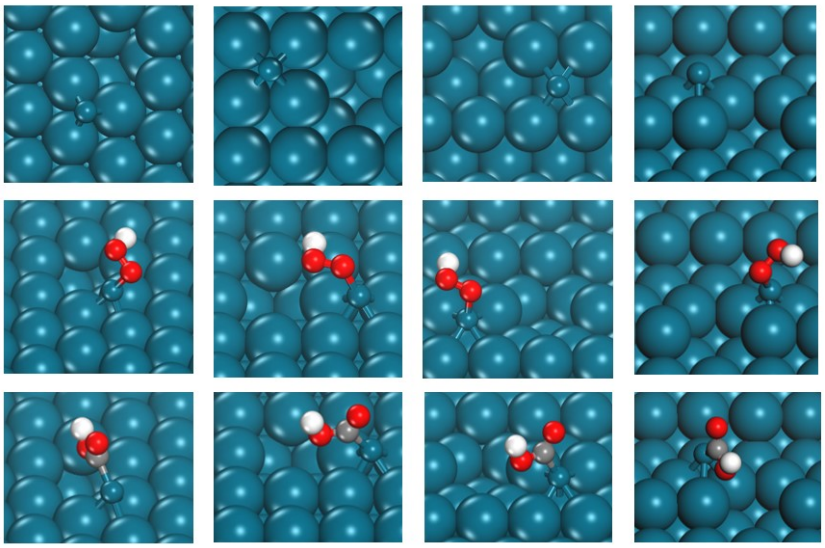

Figure S11. The optimized singe-atom vacancy on Pd(111), Pd((100), Pd((110), and Pd((211) surfaces without (top panels) and with (bottom panels) absorbed *OOH and *COOH.

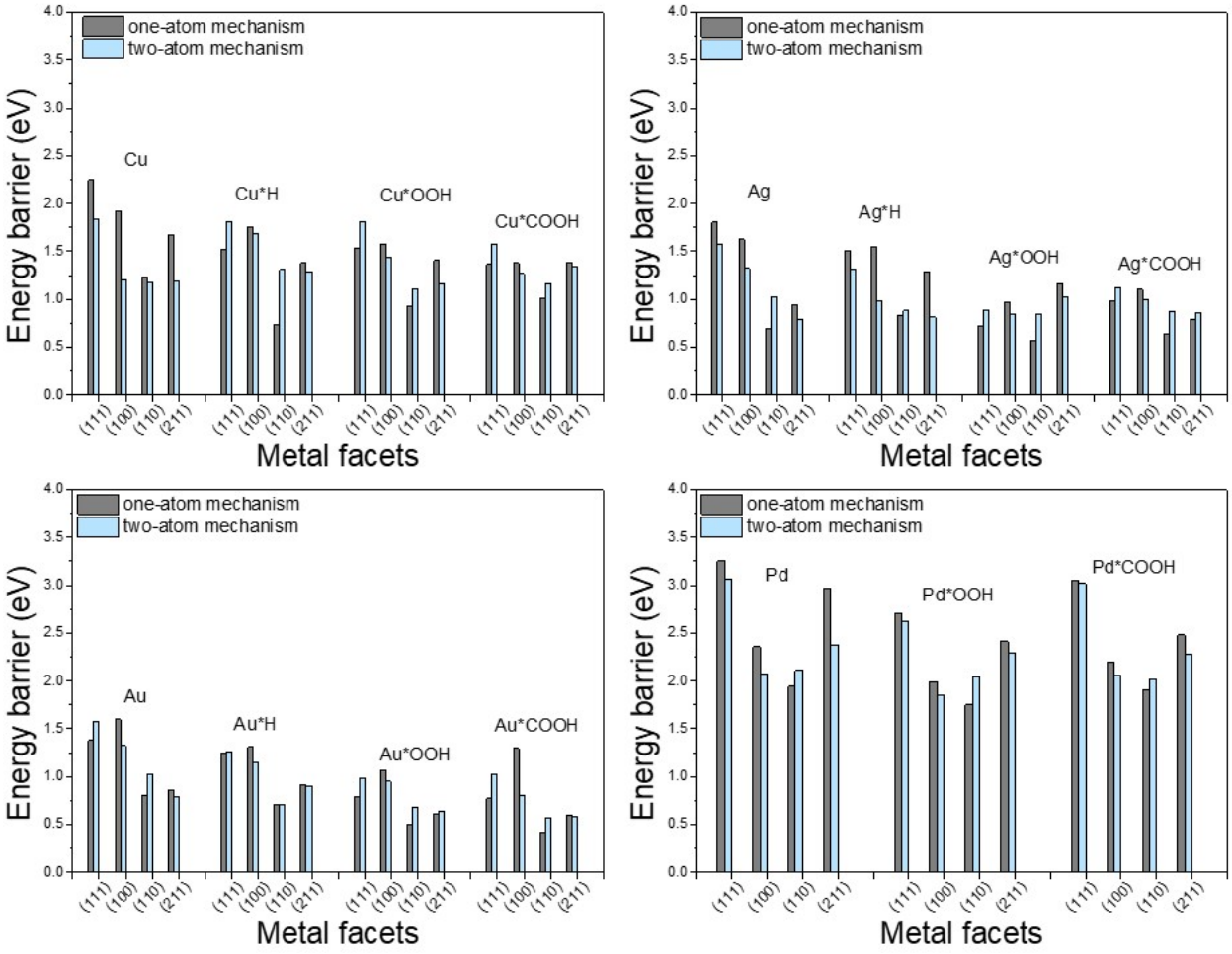

Figure S12. Comparison of the kinetic barriers for the two VF mechanisms on (111), (100), (110), and (211) surfaces of Cu, Ag, Au, and Pd.

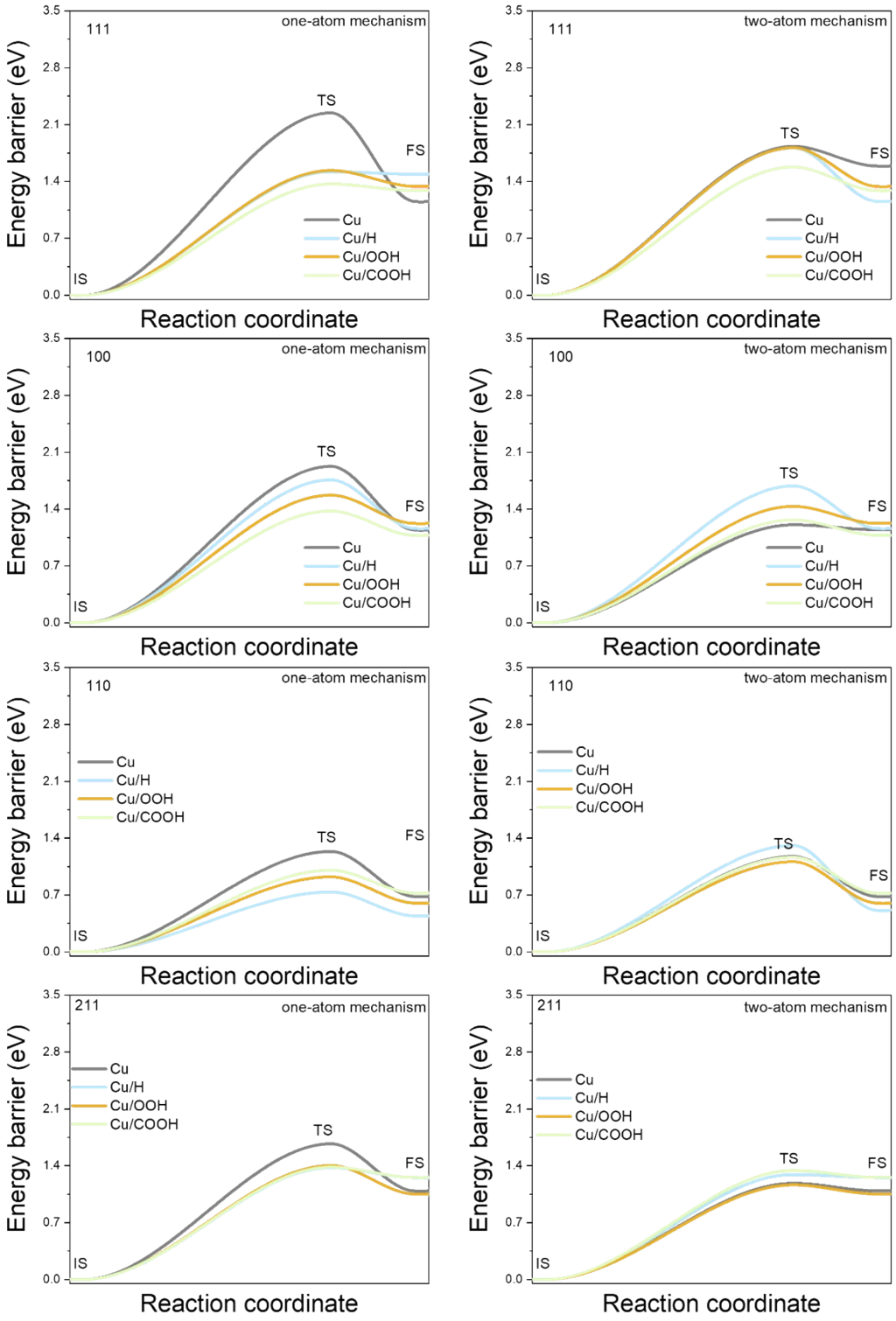

Figure S13. The calculated kinetic barriers of two VF mechanisms on Cu(111), Cu(100), Cu(110), and Cu(211) surfaces.

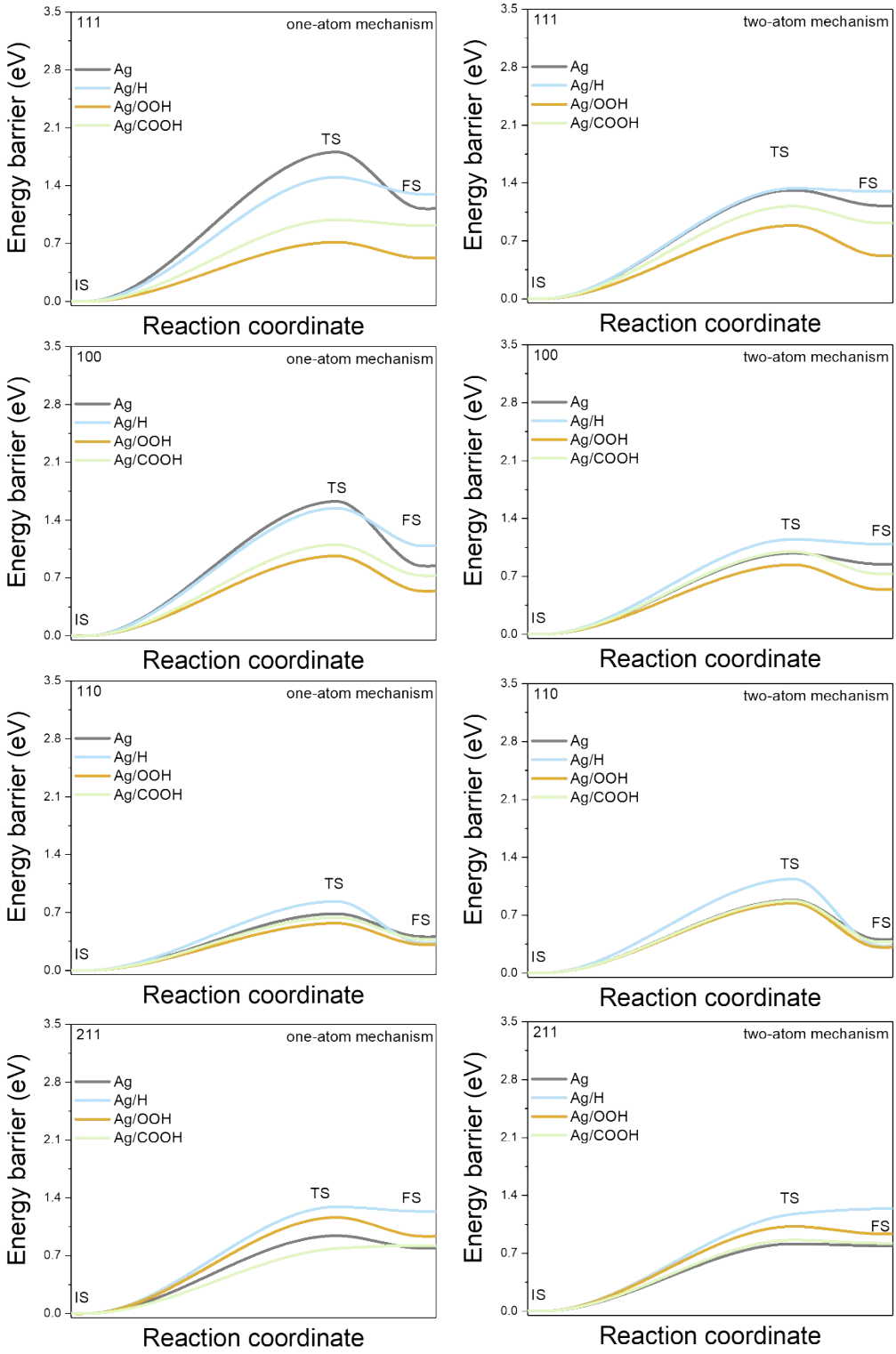

Figure S14. The calculated kinetic barriers of two VF mechanisms on Ag(111), Ag(100), Ag(110), and Ag(211) surfaces.

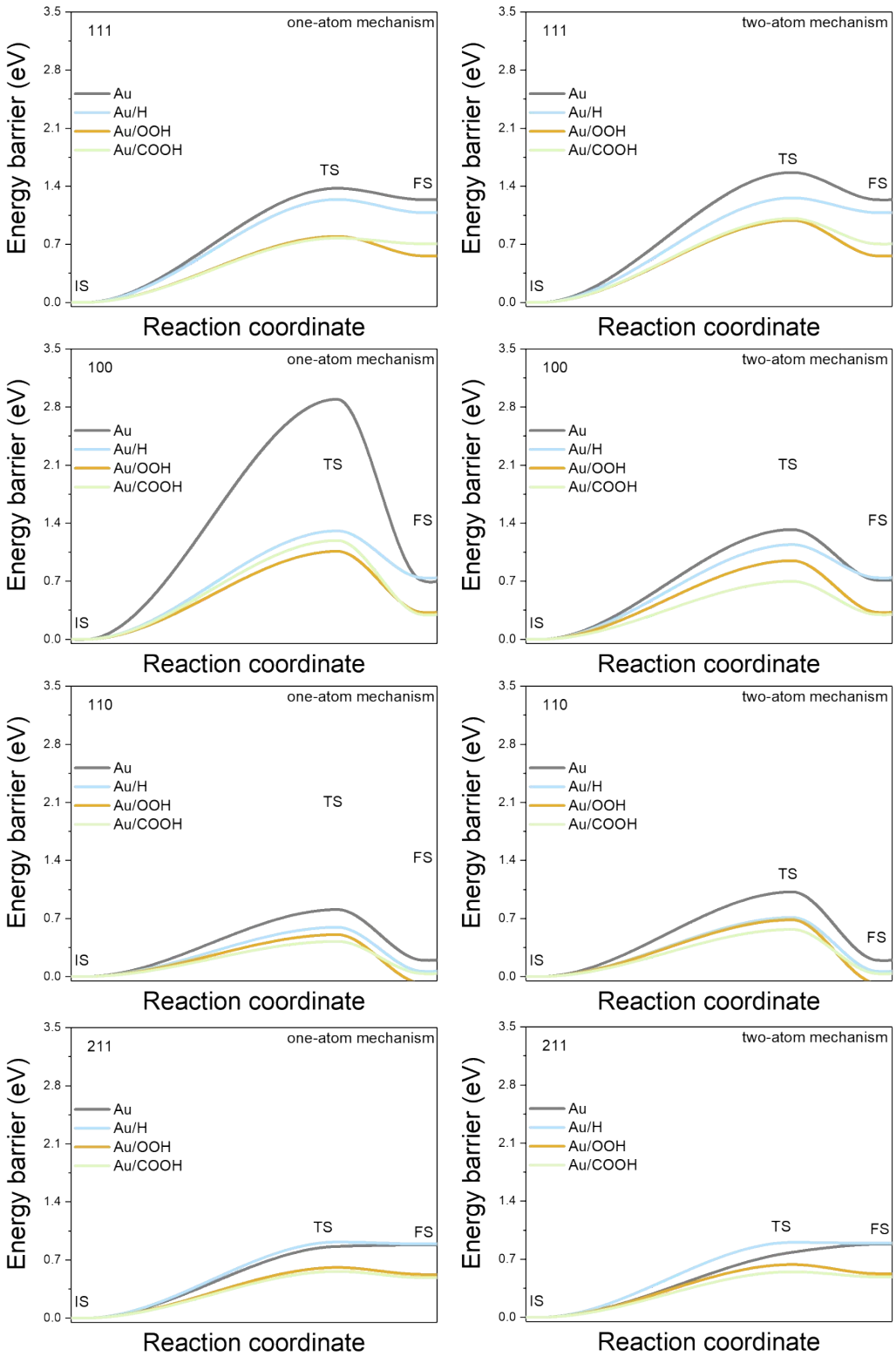

Figure S15. The calculated kinetic barriers of two VF mechanisms on Au(111), Au(100), Au(110), and Au(211) surfaces.

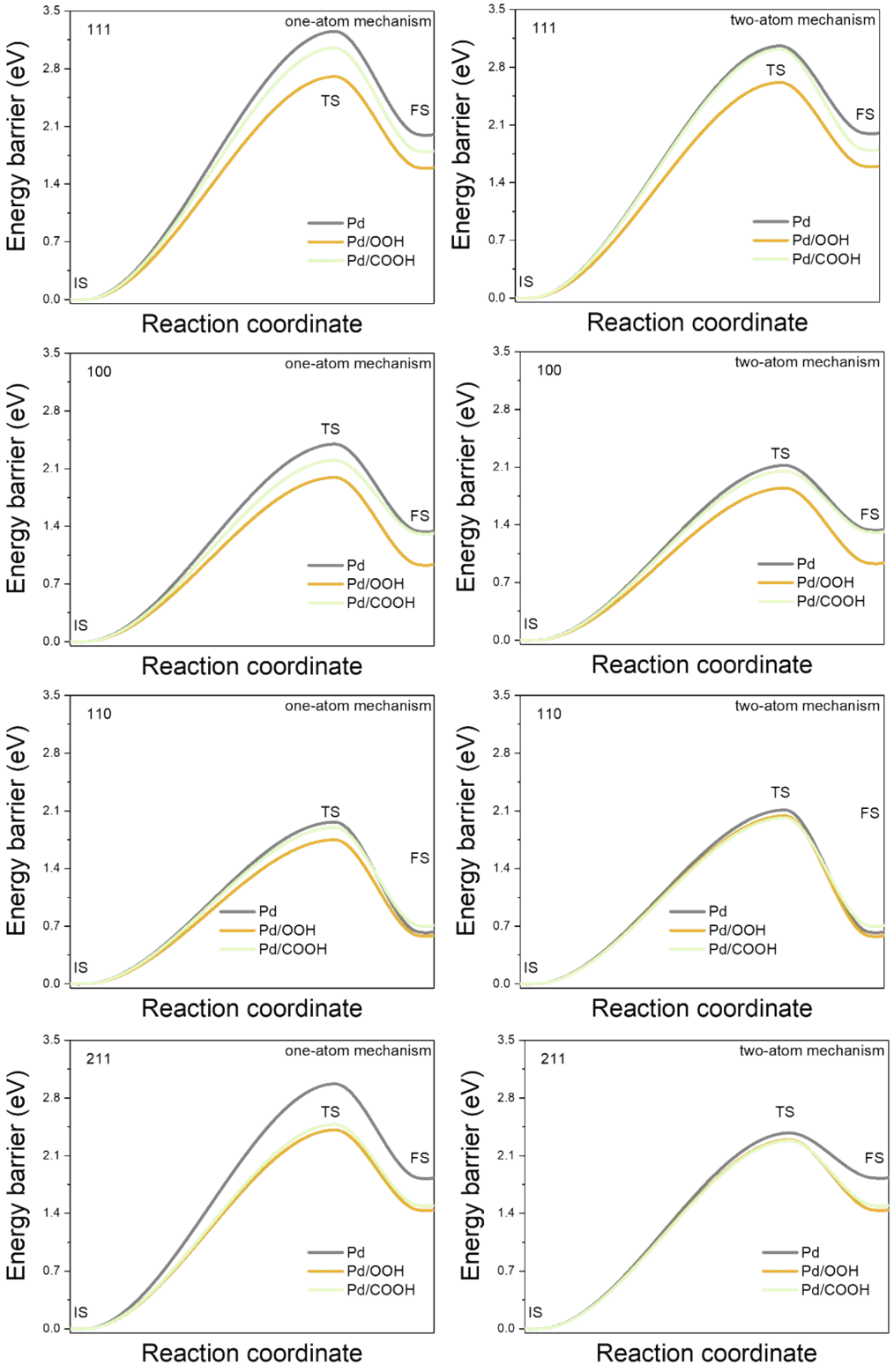

Figure S16. The calculated kinetic barriers of two VF mechanisms on Pd(111), Pd(100), Pd(110), and Pd(211) surfaces.

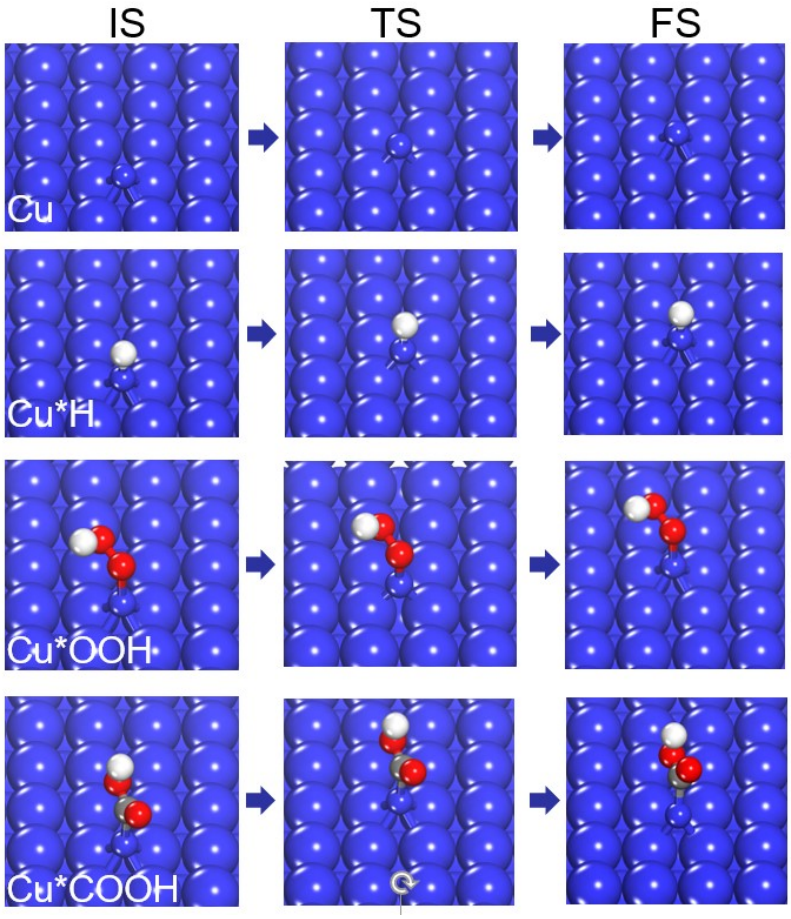

Figure S17. Optimized geometry structures for initial, transition, and final states of migration for Cu atom and intermediate-bound Cu atoms of Cu*H (HER), Cu*OOH (ORR), and Cu*COOH (CO_2RR) on the Cu(100) surface.

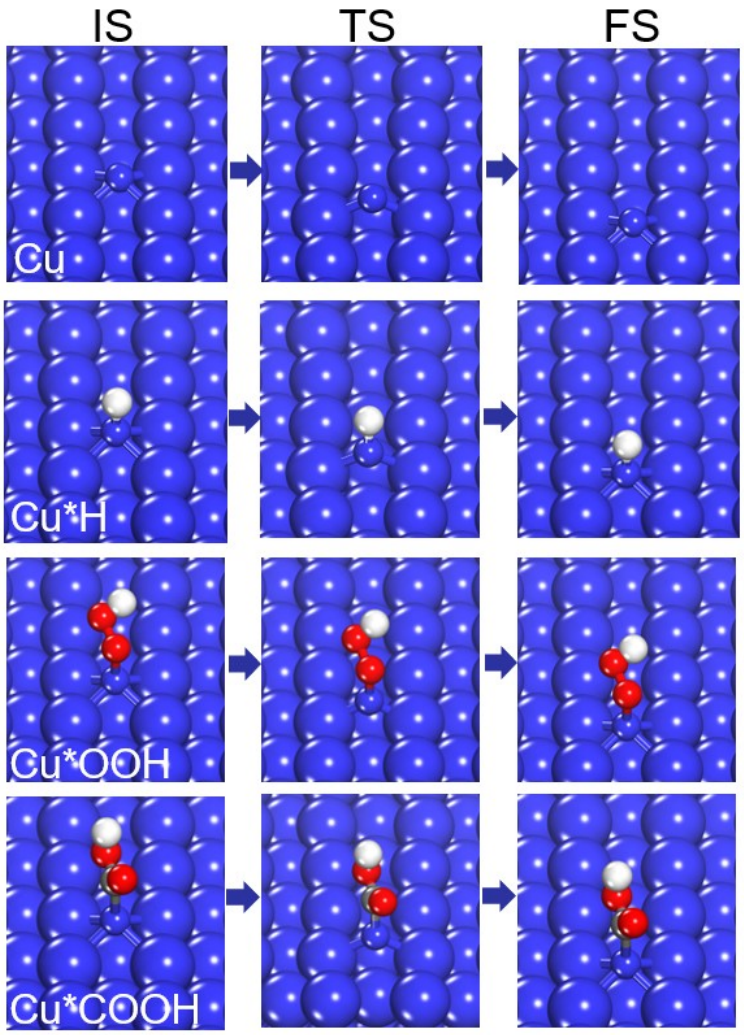

Figure S18. Optimized geometry structures for initial, transition and final states of migration for Cu atom and intermediate-bound Cu atoms of Cu*H (HER), Cu*OOH (ORR), and Cu*COOH (CO_2RR) on the Cu(110) surface.

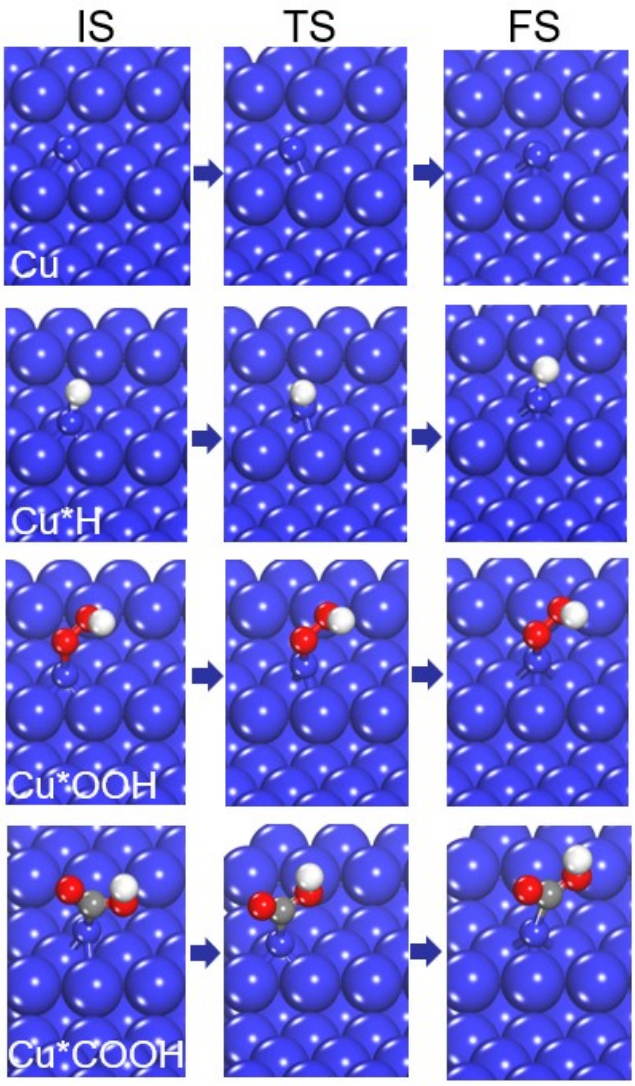

Figure S19. Optimized geometry structures for initial, transition and final states of migration for Cu atom and intermediate-bound Cu atoms of Cu*H (HER), Cu*OOH (ORR), and Cu*COOH (CO_2RR) on the Cu(211) surface.

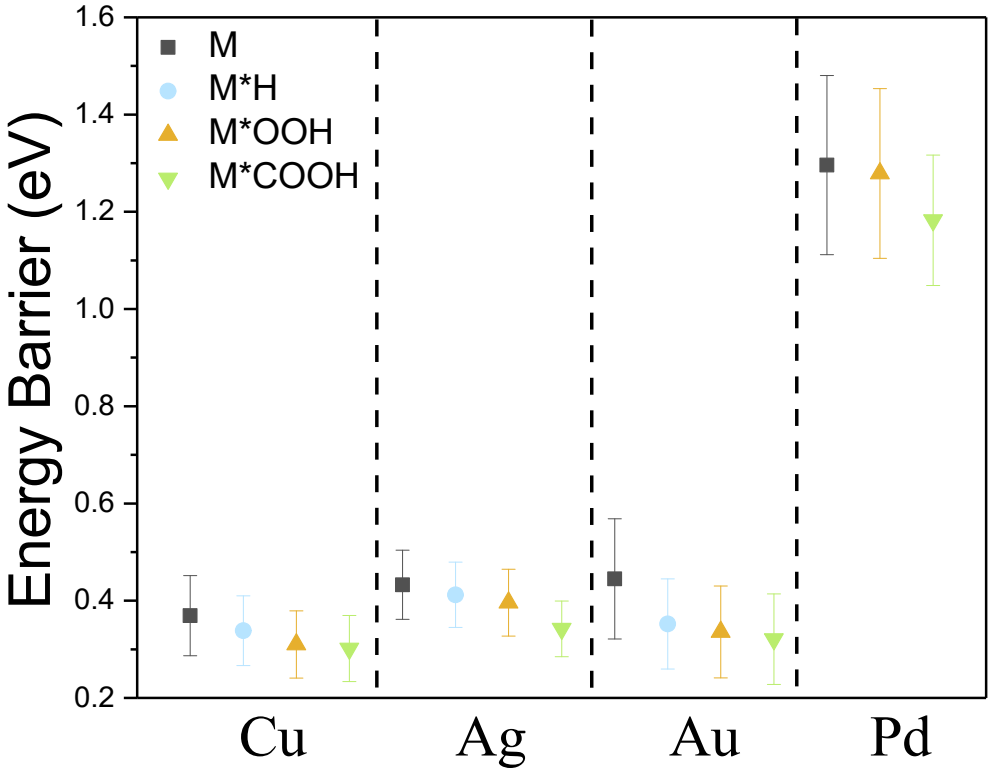

Figure S20. Average values of adatom migration energy barriers on studied four metal surfaces for Cu, Ag, Au, and Pd without and with different adsorbed RIs (*H, *OOH, and *COOH).

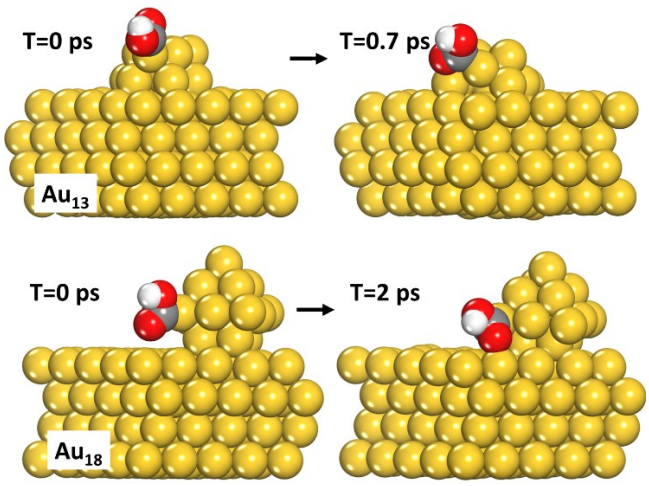

Figure S21. Snapshots during the trajectories of AIMD for Au_{13} and Au_{18} cluster with adsorbed reaction intermediate of *COOH.

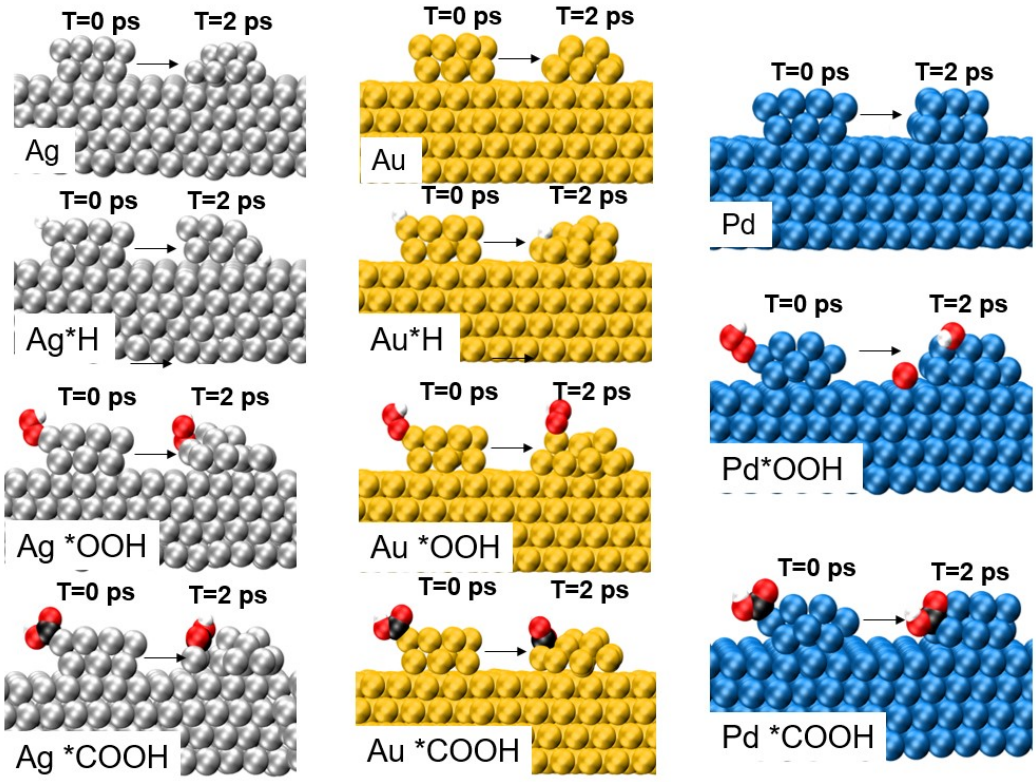

Figure S22. Snapshots during the trajectories of AIMD for Ag, Au, Pd clusters with and without adsorbed reaction intermediates of *H, *OOH, and *COOH.

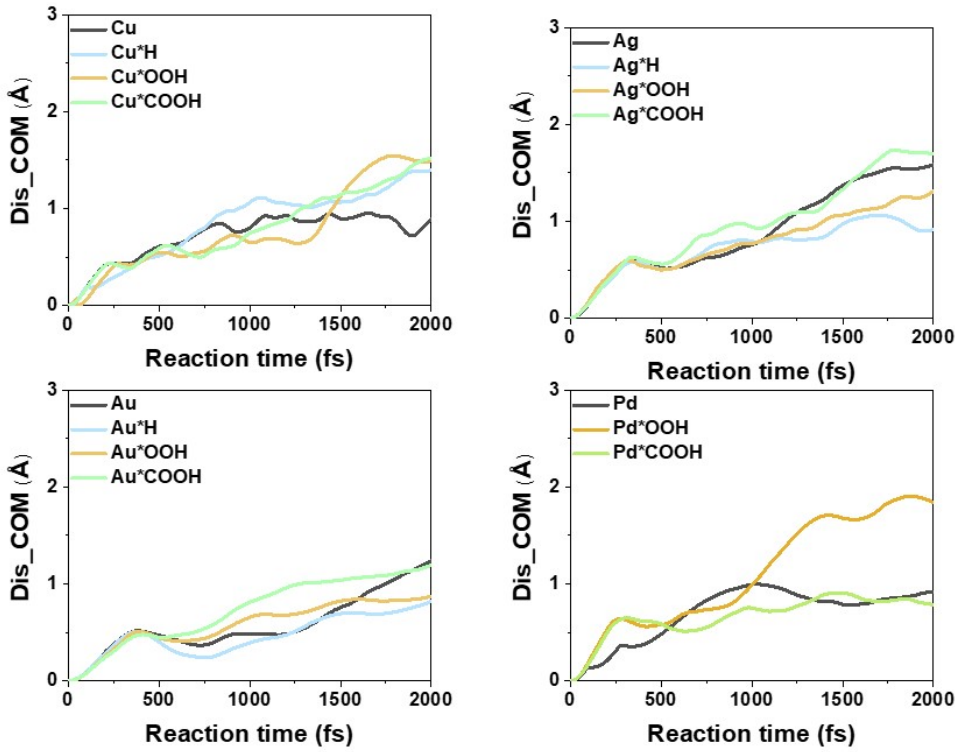

Figure S23. The change of the centre of mass for Cu, Ag, Au, and Pd clusters with and without bound RIs with time.

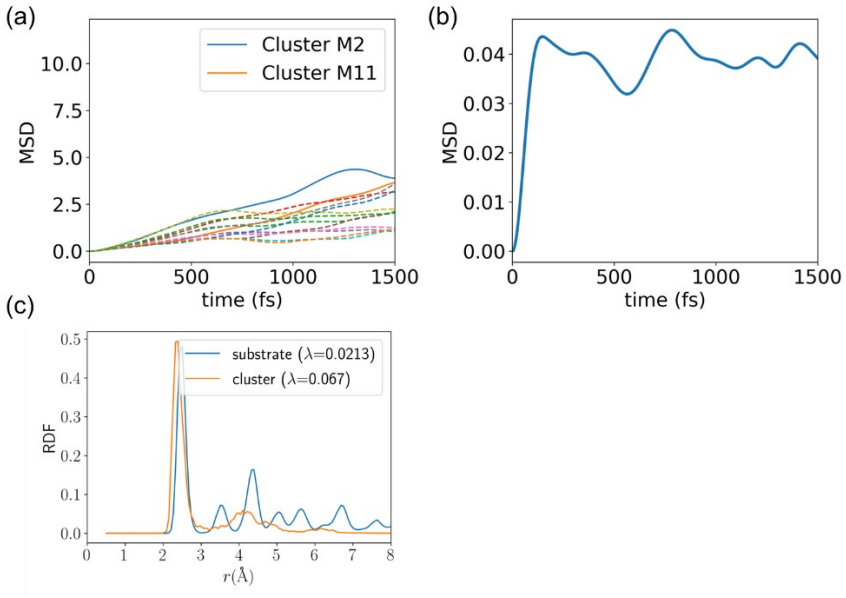

Figure S24. Profiles of time-averaged mean-square displacement (TA-MSD) and radial distribution function (RDF) for Cu cluster supported on Cu(111) surface. (a) TA-MSDs for cluster Cu atoms. TA-MSD

for the first 2 most mobily cluster atoms is shown in solid line, with the rest shown in dash line. (b) Averaged TA-MSD for all substrate metal atoms. (c) RDF and Lindemann index of the metal cluster and substrate.

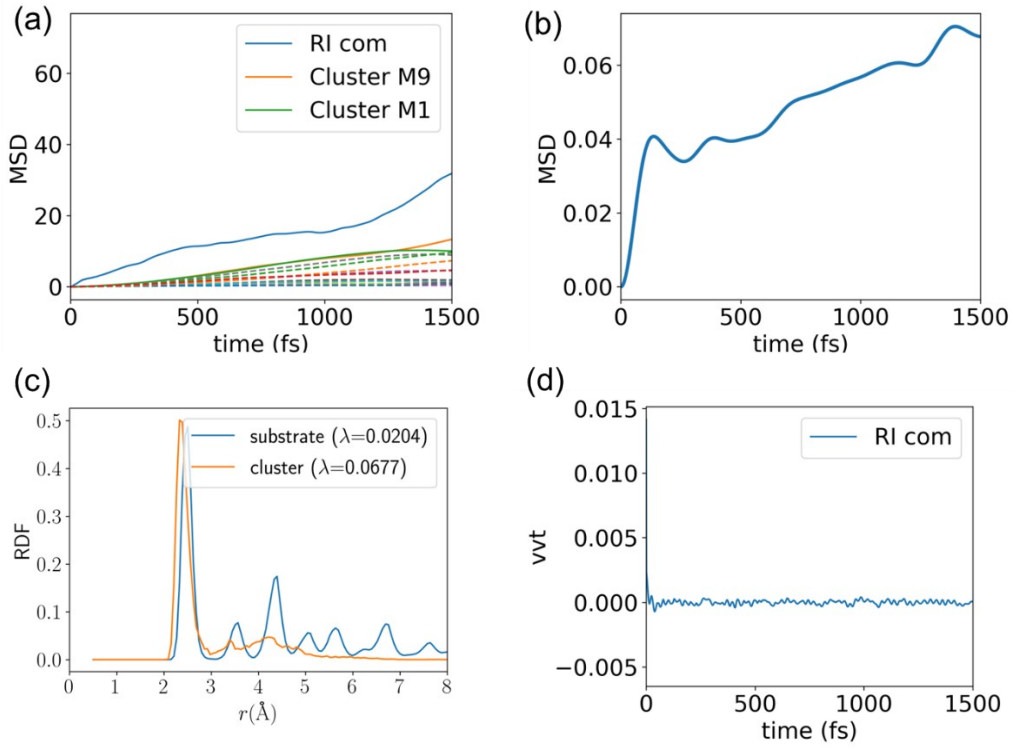

Figure S25. Profiles of time-averaged mean-square displacement (TA-MSD), radial distribution function (RDF), and vvt for H-bound Cu cluster supported on Cu(111) surface. (a) TA-MSDs for cluster Cu atoms. TA-MSD for the first 2 most mobily cluster atoms is shown in solid line, with the rest shown in dash line. (b) Averaged TA-MSD for all substrate metal atoms. (c) RDF and Lindemann index of the metal cluster and substrate, and the RDF of the reaction intermediate. (d) vvt for reaction intermediate of H.

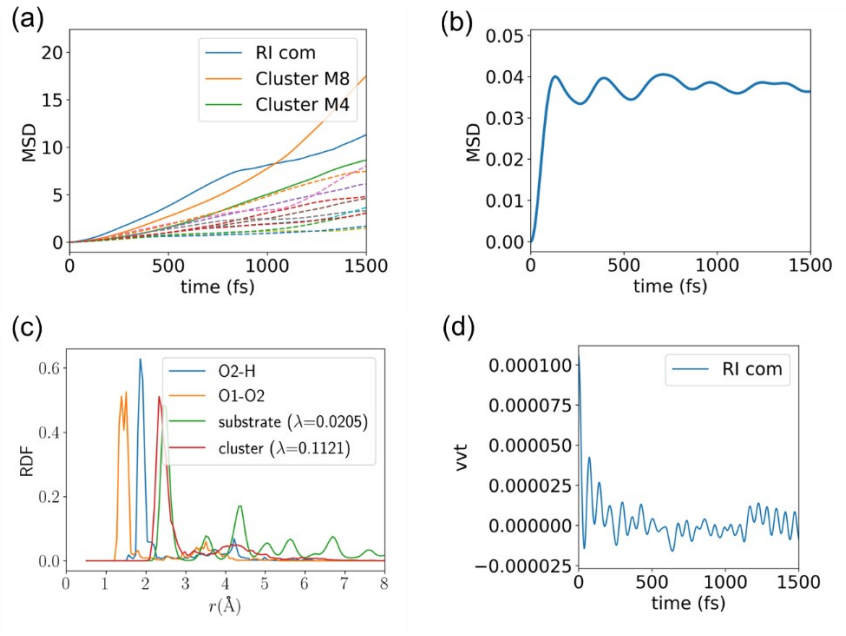

Figure S26. Profiles of time-averaged mean-square displacement (TA-MSD), radial distribution function (RDF), and vvt for OOH-bound Cu cluster supported on Cu(111) surface. (a) TA-MSDs for cluster Cu atoms. TA-MSD for the first 2 most mobily cluster atoms is shown in solid line, with the rest shown in dash line. (b) Averaged TA-MSD for all substrate metal atoms. (c) RDF and Lindemann index of the metal cluster and substrate, and RDF of the reaction intermediate. (d) vvt for reaction intermediate of OOH.

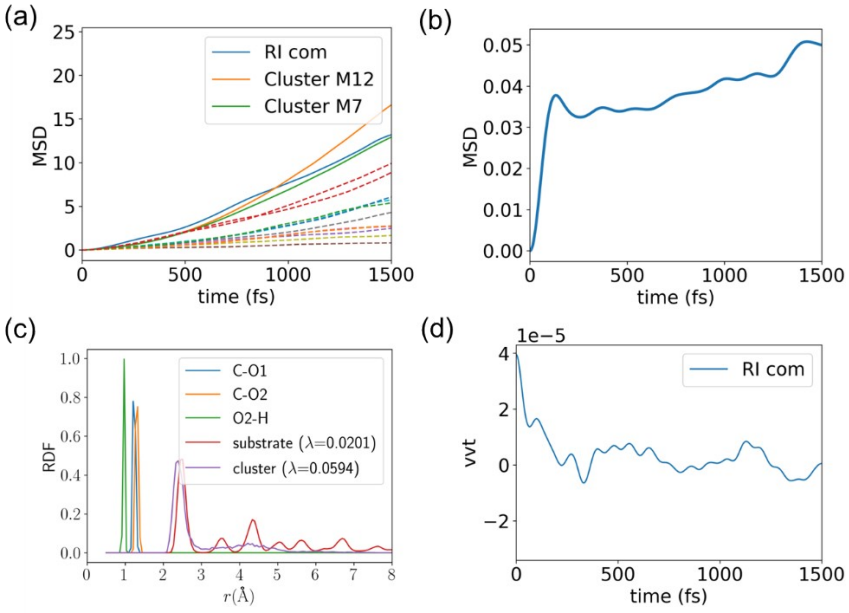

Figure S27. Profiles of time-averaged mean-square displacement (TA-MSD), radial distribution function (RDF), and vvt for COOH-bound Cu cluster supported on Cu(111) surface. (a) TA-MSDs for cluster Cu atoms. TA-MSD for the first 2 most mobily cluster atoms is shown in solid line, with the rest shown in dash line. (b) Averaged TA-MSD for all substrate metal atoms. (c) RDF and Lindemann index of the metal cluster and substrate, and the RDF of the reaction intermediate. (d) vvt for reaction intermediate of COOH.

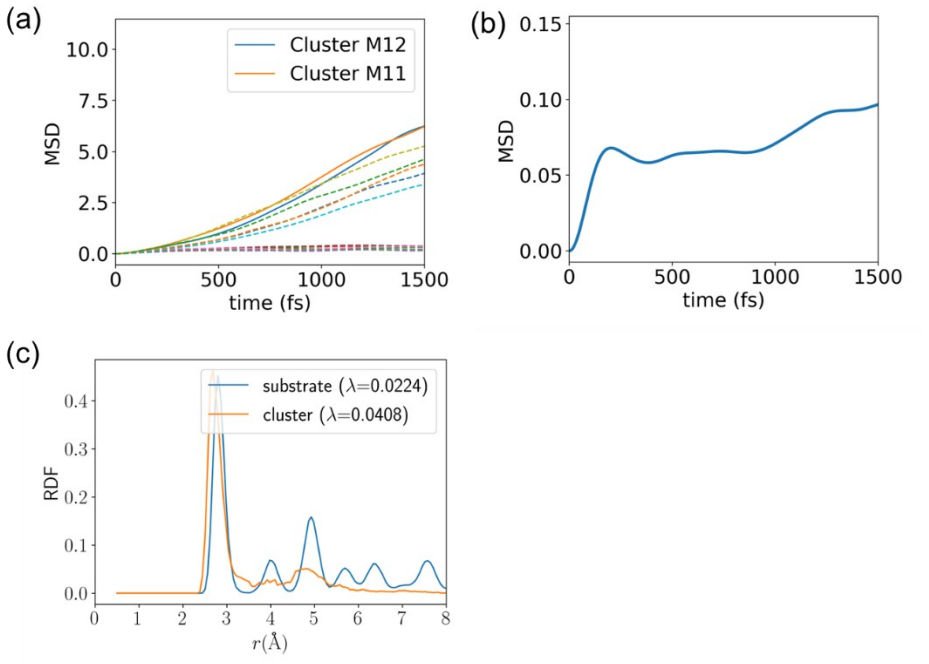

Figure S28 Profiles of time-averaged mean-square displacement (TA-MSD) and radial distribution function (RDF) for Ag cluster supported on Ag(111) surface. (a) TA-MSDs for cluster Ag atoms. TA-MSD for the first 2 most mobily cluster atoms is shown in solid line, with the rest shown in dash line. (b) Averaged TA-MSD for all substrate metal atoms. (c) RDF and Lindemann index of the metal cluster and substrate.

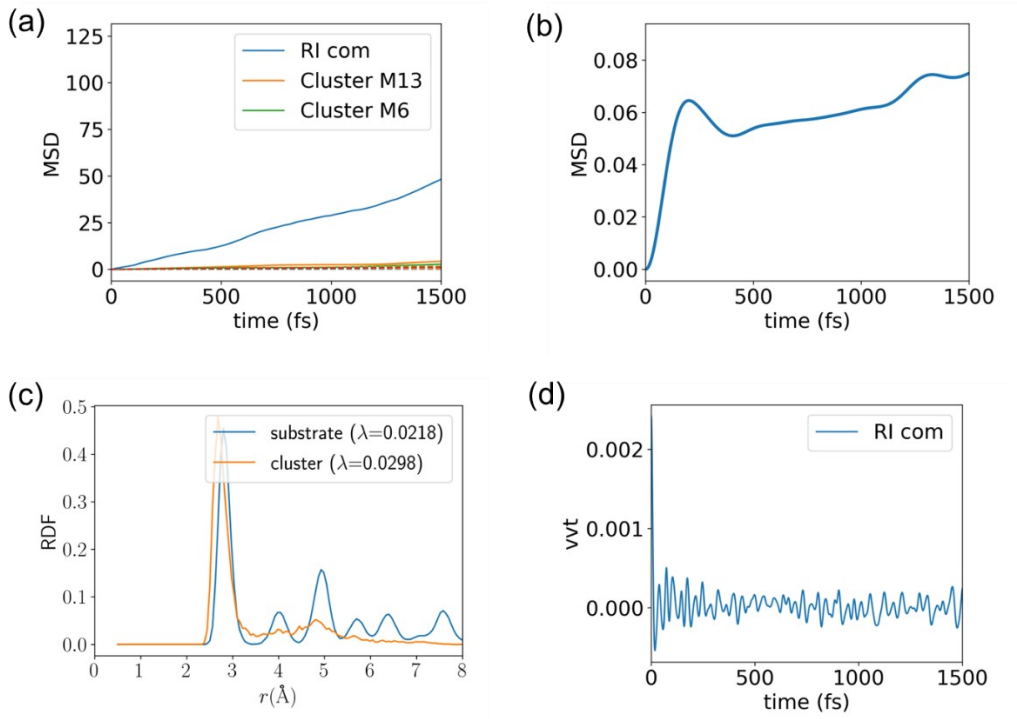

Figure S29. Profiles of time-averaged mean-square displacement (TA-MSD), radial distribution function (RDF), and vvt for H-bound Ag cluster supported on Ag(111) surface. (a) TA-MSDs for cluster Ag atoms. TA-MSD for the first 2 most mobily cluster atoms is shown in solid line, with the rest shown in dash line. (b) Averaged TA-MSD for all substrate metal atoms. (c) RDF and Lindemann index of the metal cluster and substrate, and the RDF of the reaction intermediate. (d) vvt for reaction intermediate of H.

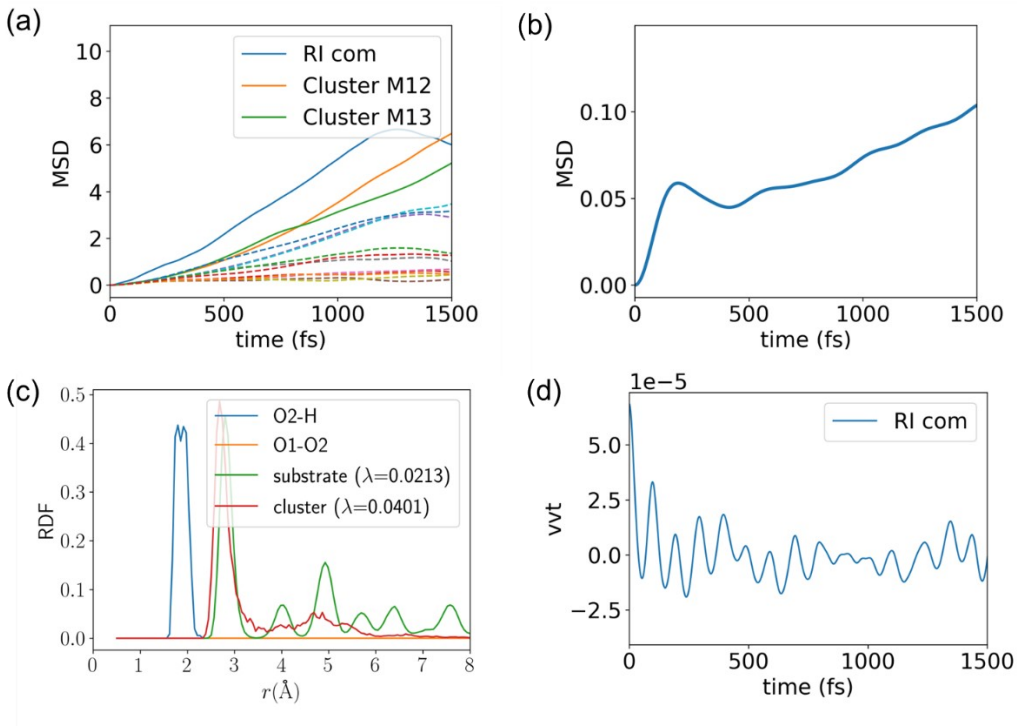

Figure S30. Profiles of time-averaged mean-square displacement (TA-MSD), radial distribution function (RDF), and vvt for OOH-bound Ag cluster supported on Ag(111) surface. (a) TA-MSDs for cluster Ag atoms. TA-MSD for the first 2 most mobily cluster atoms is shown in solid line, with the rest shown in dash line. (b) Averaged TA-MSD for all substrate metal atoms. (c) RDF and Lindemann index of the metal cluster and substrate, and the RDF of the reaction intermediate. (d) vvt for reaction intermediate of OOH.

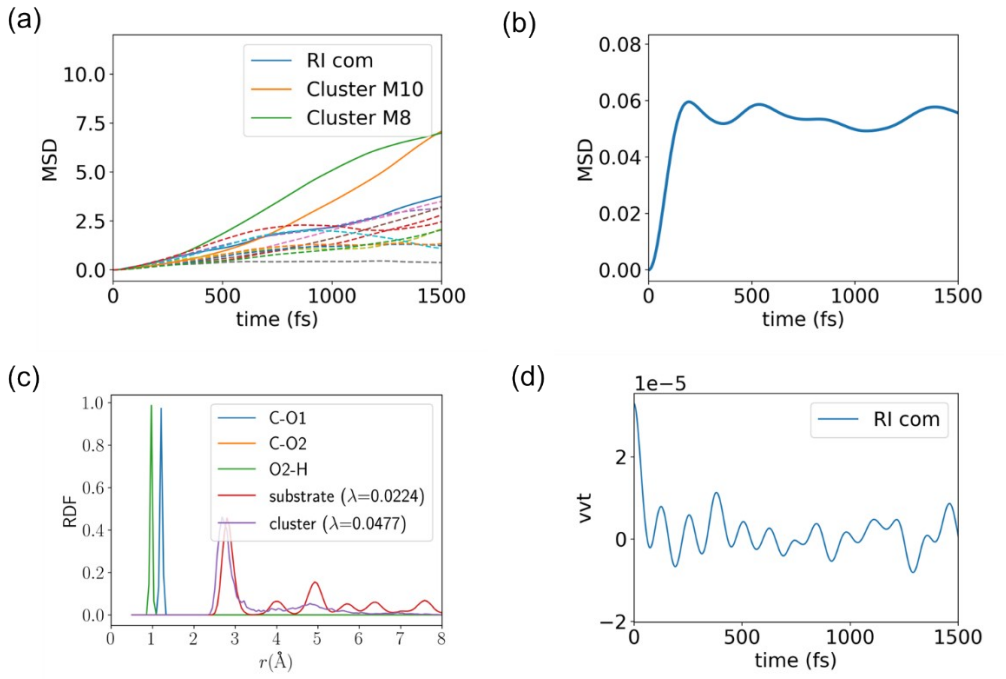

Figure S31. Profiles of time-averaged mean-square displacement (TA-MSD), radial distribution function (RDF), and vvt for COOH-bound Ag cluster supported on Ag(111) surface. (a) TA-MSDs for cluster Ag atoms. TA-MSD for the first 2 most mobily cluster atoms is shown in solid line, with the rest shown in dash line. (b) Averaged TA-MSD for all substrate metal atoms. (c) RDF and Lindemann index of the metal cluster and substrate, and the RDF of the reaction intermediate. (d) vvt for reaction intermediate of OOH.

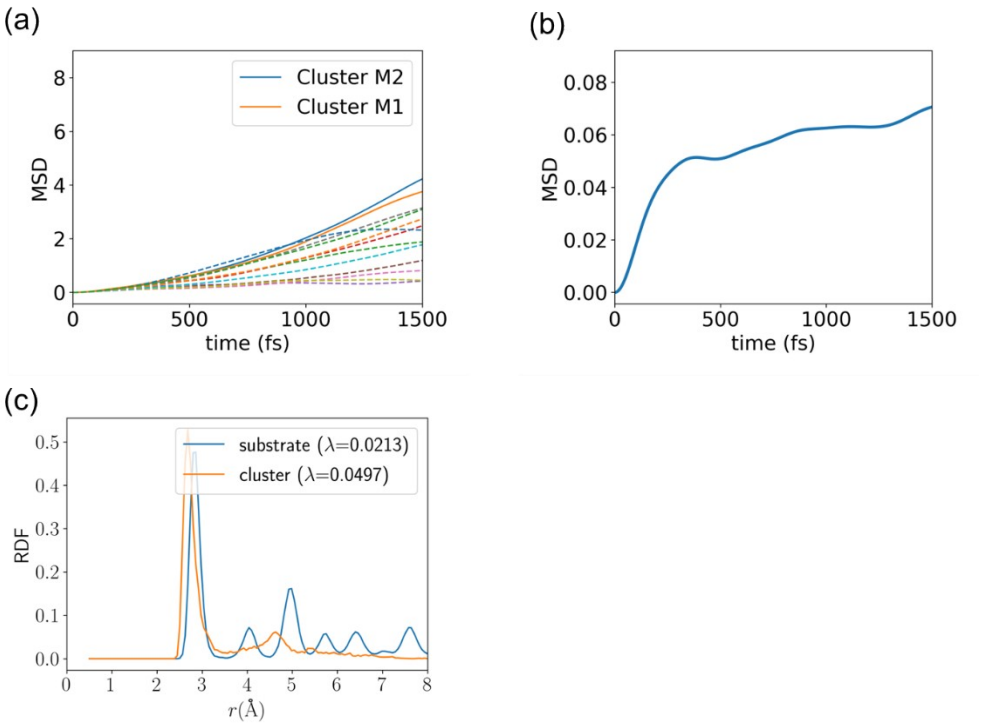

Figure S32. Profiles of time-averaged mean-square displacement (TA-MSD) and radial distribution function (RDF) for Au cluster supported on Au(111) surface. (a) TA-MSDs for cluster Au atoms. TA-MSD for the first 2 most mobily cluster atoms is shown in solid line, with the rest shown in dash line. (b) Averaged TA-MSD for all substrate metal atoms. (c) RDF and Lindemann index of the metal cluster and substrate.

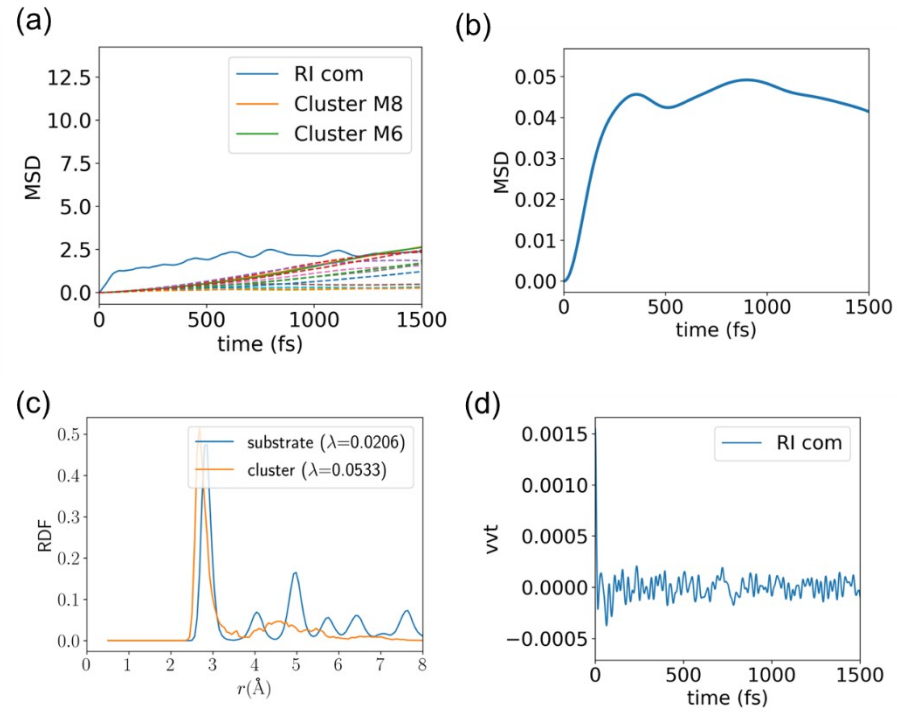

Figure S33. Profiles of time-averaged mean-square displacement (TA-MSD), radial distribution function (RDF), and vvt for H-bound Au cluster supported on Au(111) surface. (a) TA-MSDs for cluster Au atoms. TA-MSD for the first 2 most mobily cluster atoms is shown in solid line, with the rest shown in dash line. (b) Averaged TA-MSD for all substrate metal atoms. (c) RDF and Lindemann index of the metal cluster and substrate, and the RDF of the reaction intermediate. (d) vvt for reaction intermediate of H.

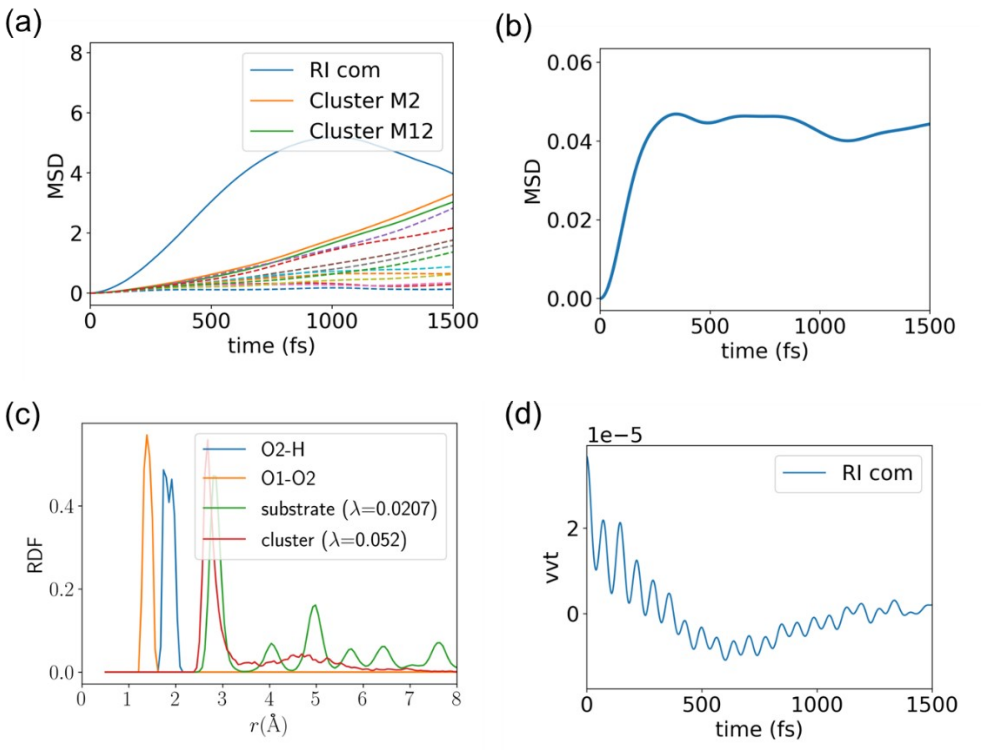

Figure S34. Profiles of time-averaged mean-square displacement (TA-MSD), radial distribution function (RDF), and vvt for OOH-bound Au cluster supported on Au(111) surface. (a) TA-MSDs for cluster Au atoms. TA-MSD for the first 2 most mobily cluster atoms is shown in solid line, with the rest shown in dash line. (b) Averaged TA-MSD for all substrate metal atoms. (c) RDF and Lindemann index of the metal cluster and substrate, and the RDF of the reaction intermediate. (d) vvt for reaction intermediate of OOH.

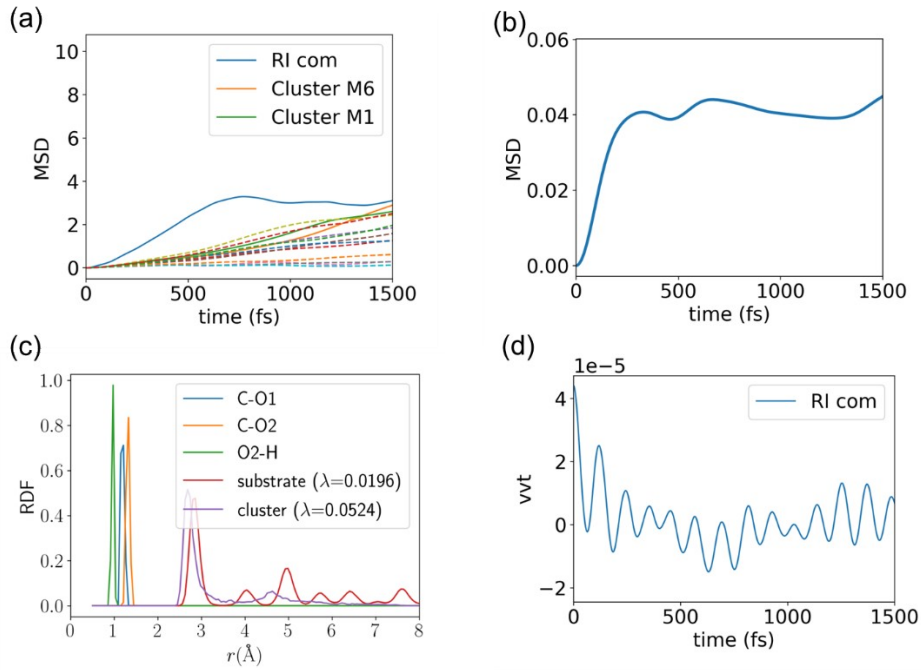

Figure S35. Profiles of time-averaged mean-square displacement (TA-MSD), radial distribution function (RDF), and vvt for COOH-bound Au cluster supported on Au(111) surface. (a) TA-MSDs for cluster Au atoms. TA-MSD for the first 2 most mobily cluster atoms is shown in solid line, with the rest shown in dash line. (b) Averaged TA-MSD for all substrate metal atoms. (c) RDF and Lindemann index of the metal cluster and substrate, and the RDF of the reaction intermediate. (d) vvt for reaction intermediate of COOH.

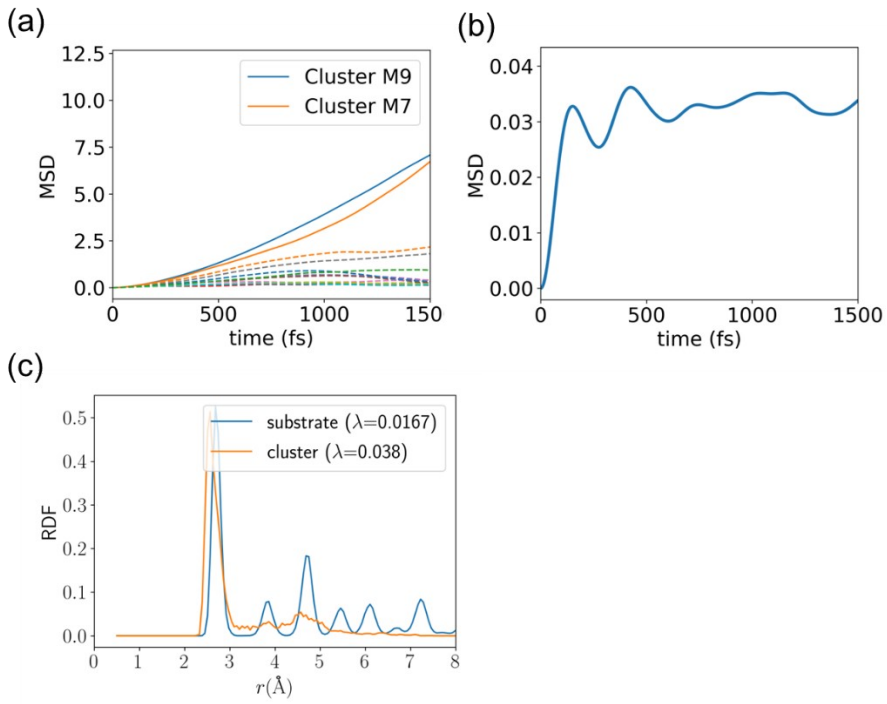

Figure S36. Profiles of time-averaged mean-square displacement (TA-MSD) and radial distribution function (RDF) for Pd cluster supported on Pd(111) surface. (a) TA-MSDs for cluster Ag atoms. TA-MSD for the first 2 most mobily cluster atoms is shown in solid line, with the rest shown in dash line. (b) Averaged TA-MSD for all substrate metal atoms. (c) RDF and Lindemann index of the metal cluster and substrate.

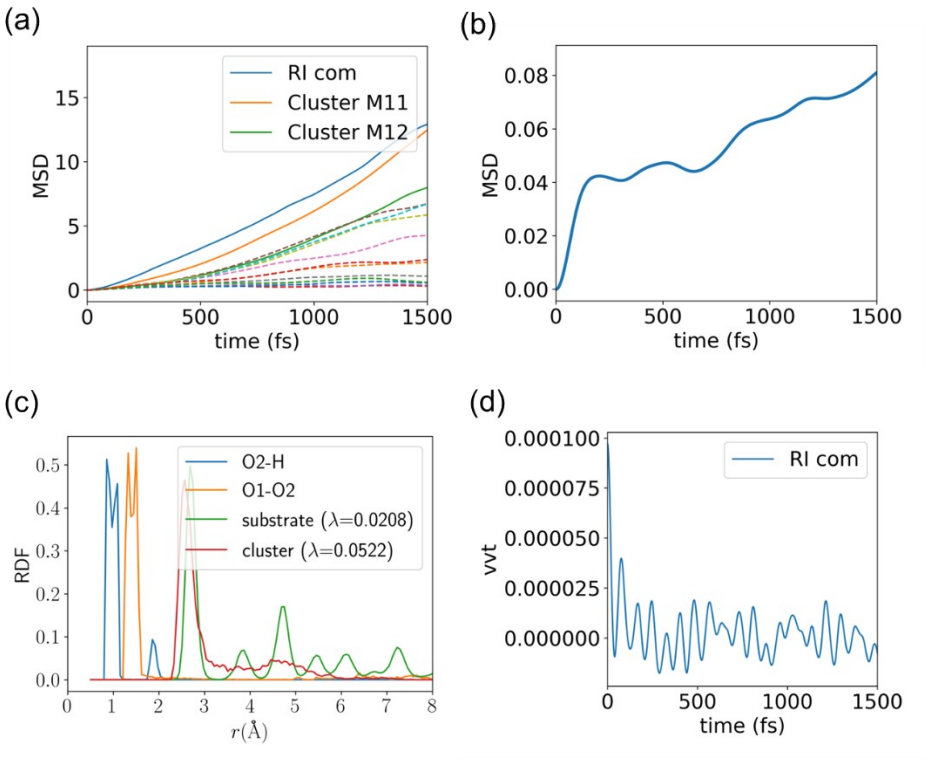

Figure S37. Profiles of time-averaged mean-square displacement (TA-MSD), radial distribution function (RDF), and vvt for OOH-bound Pd cluster supported on Pd(111) surface. (a) TA-MSDs for cluster Au atoms. TA-MSD for the first 2 most mobily cluster atoms is shown in solid line, with the rest shown in dash line. (b) Averaged TA-MSD for all substrate metal atoms. (c) RDF and Lindemann index of the metal cluster and substrate, and the RDF of the reaction intermediate. (d) vvt for reaction intermediate of OOH.

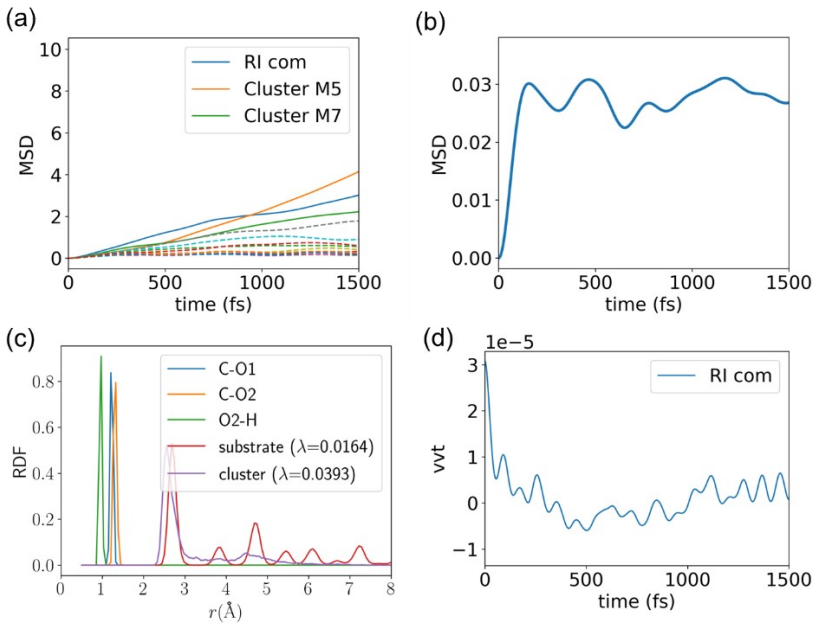

Figure S38. Profiles of time-averaged mean-square displacement (TA-MSD), radial distribution function (RDF), and vvt for COOH-bound Pd cluster supported on Pd(111) surface. (a) TA-MSDs for cluster Au atoms. TA-MSD for the first 2 most mobile cluster atoms is shown in solid line, with the rest shown in dash line. (b) Averaged TA-MSD for all substrate metal atoms. (c) RDF and Lindemann index of the metal cluster and substrate, and the RDF of the reaction intermediate. (d) vvt for reaction intermediate of COOH.

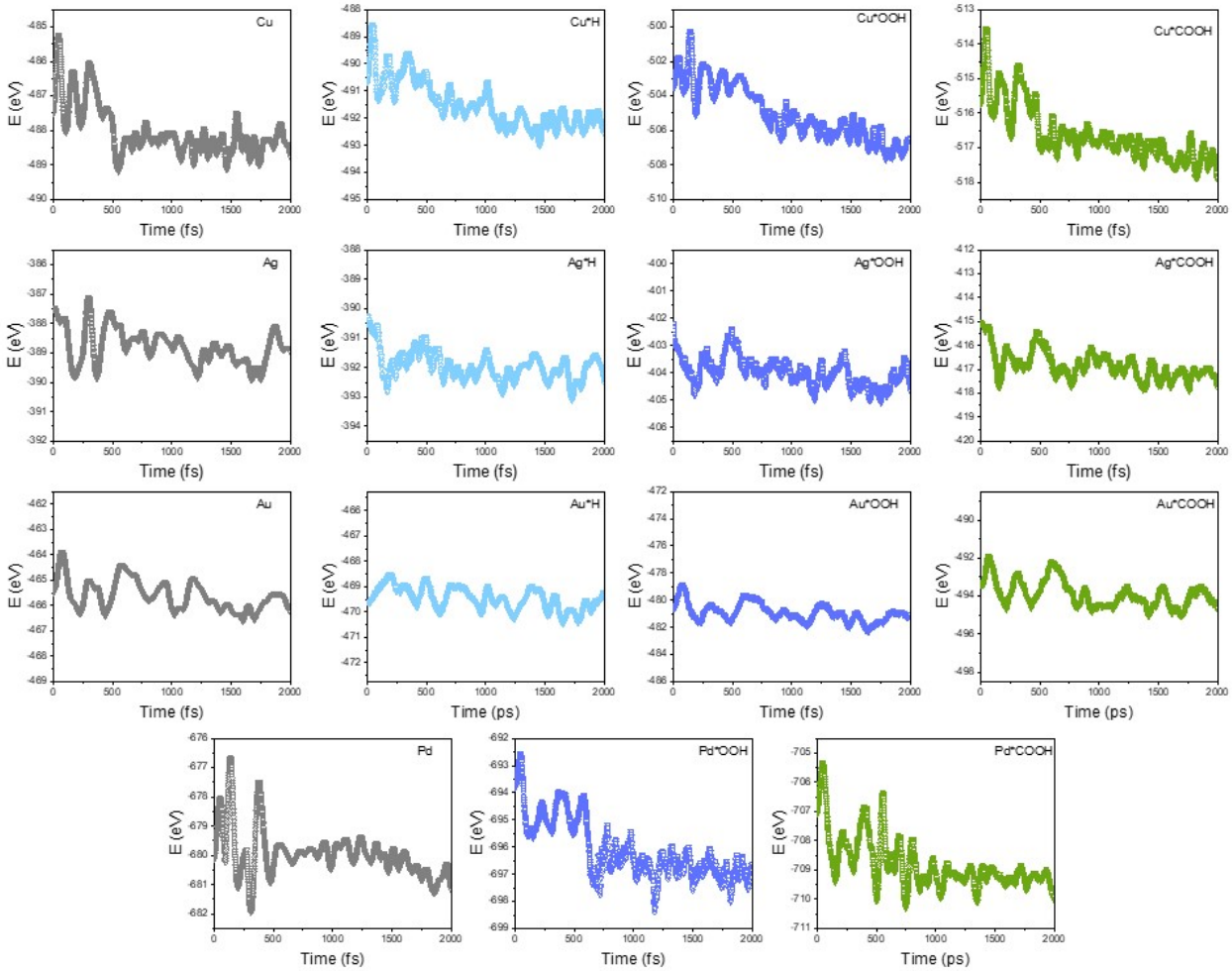

Figure S39. The electronic energy profile as a function of time for Cu, Ag, Au, and Pd clusters with and without adsorbed reaction intermediates.

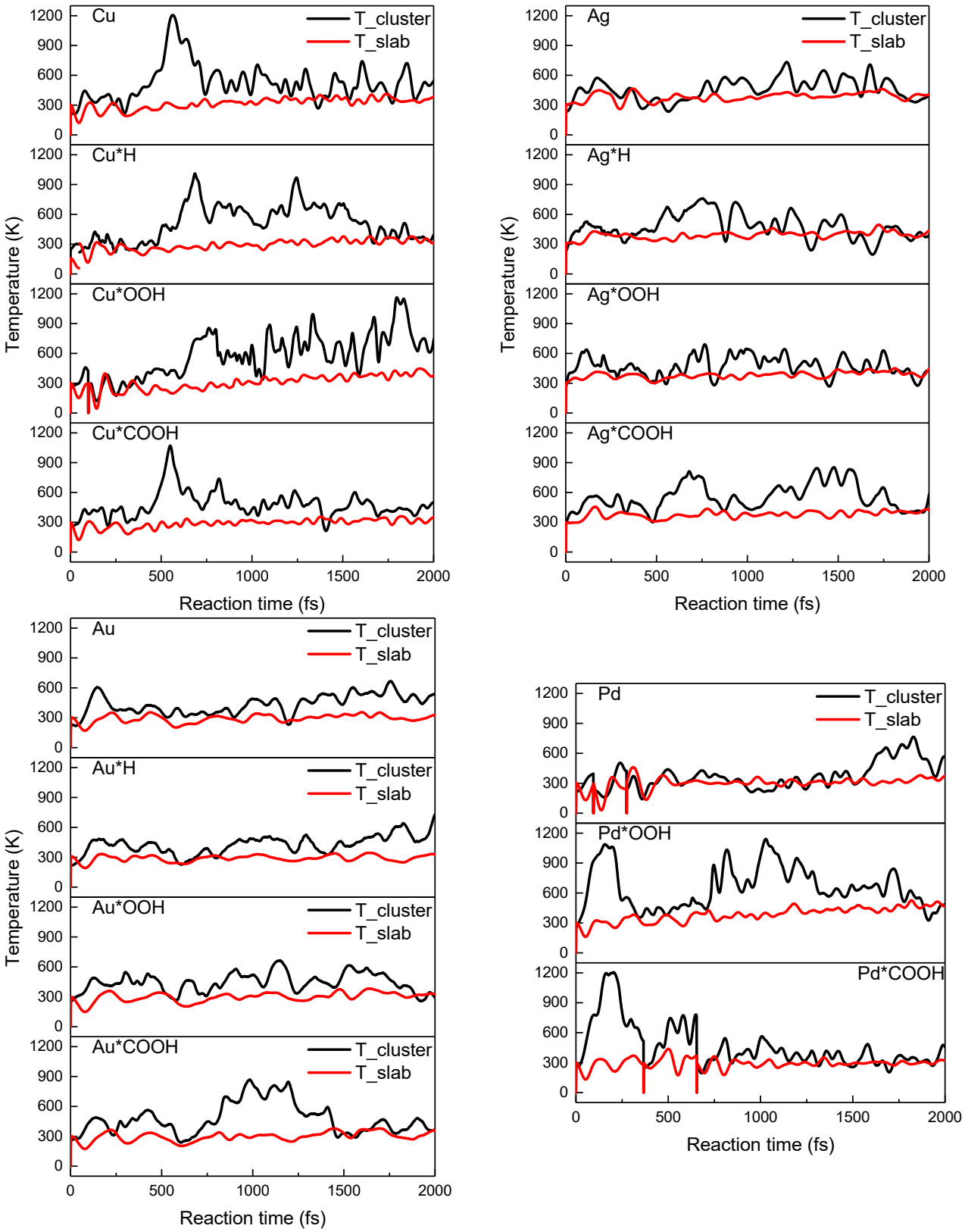

Figure S40. The temperature change of metal cluster and slab as a function of simulation time.

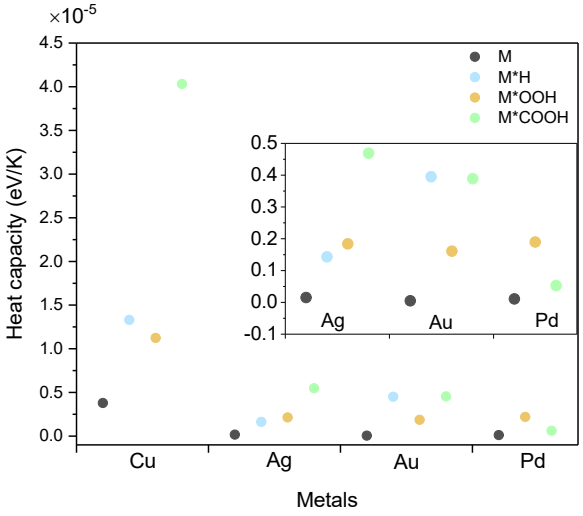

Figure S41. The heat capacities of Cu, Ag, Au, and Pd cluster systems.

References：

1 S. L. Gafner, L. V. Redel and Y. Y. Gafner, *J. Exp. Theor. Phys.*, 2009, **108**, 784.

2 *CRC Handbook of Chemistry and Physics*, 102nd Edit.; Rumble, J. R., Ed.; CRC Press/Taylor & Francis, Boca Raton, 2021.

3 D. K. Pattadar and F. P. Zamborini, *J. Am. Chem. Soc.*, 2018, **140**, 14126.

4 R. G. Capelo, L. Leppert and R. Q. Albuquerque, *J. Phys. Chem. C*, 2014, **118**, 21647.

5 P. L. Redmond, A. J. Hallock and L. E. Brus, *Nano Lett.*, 2005, **5**, 131.